REPORT DOCUMENTATION PAGE

AFRL-SR-BL-TR-01-

0319

1. AGENCY USE ONLY *(Leave blank)*	2. REPORT DATE	3. REPORT TYPE AND DATES COVERED
	18 Apr 01	FINAL REPORT 01 Aug 97 TO 30 Sep 00

4. TITLE AND SUBTITLE
DEMONSTRATION OF ROBUST MICROMACHINED JET TECHNOLOGY AND ITS APPLICATION TO REALISTIC FLOW CONTROL PROBLEMS

5. FUNDING NUMBERS
F49620-97-1-0519

6. AUTHOR(S)
Prof. Mark G. Allen
Prof. Ari Glezer

7. PERFORMING ORGANIZATION NAME(S) AND ADDRESS(ES)
GEORGIA INSTITUTE OF TECHNOLOGY
Training & Technologies
Atlanta, GA 30332-0420

8. PERFORMING ORGANIZATION REPORT NUMBER

9. SPONSORING/MONITORING AGENCY NAME(S) AND ADDRESS(ES)
AFOSR/NA
801 N. Randolph St.
Arlington VA 22203

10. SPONSORING/MONITORING AGENCY REPORT NUMBER

11. SUPPLEMENTARY NOTES

12a. DISTRIBUTION AVAILABILITY STATEMENT

Cleared for public distribution

13. ABSTRACT *(Maximum 200 words)*

In this work, we are investigating the use of microfabrication technology to create a micromachined fluidic control system (consisting of micromachined actuators, sensors, and control/drive circuitry) with a goal of application in practical fluids problems, such as UAV-scale aerodynamic control. Our approaches include: (1) the development of suitable micromachined synthetic jets (microjets) as actuators, which obviate the need to physically extend micromachined structures into an external flow; and (2) a non-silicon alternative micromachining fabrication technology based on metallic substraits and lamination (in addition to traditional MEMS technologies) which will allow the realization of larger scale, more robust structures and larger array active areas for fluidic systems.

14. SUBJECT TERMS
ROBUST MICROMACHINED JET TECHNOLOGY

15. NUMBER OF PAGES

16. PRICE CODE

17. SECURITY CLASSIFICATION OF REPORT	18. SECURITY CLASSIFICATION OF THIS PAGE	19. SECURITY CLASSIFICATION OF ABSTRACT	20. LIMITATION OF ABSTRACT
UNCLASSIFIED	UNCLASSIFIED	UNCLASSIFIED	UL

Demonstration of Robust Micromachined Jet Technology and its Application to Realistic Flow Control Problems

AFOSR GRANT F49620-97-1-0519

Final Report

Compiled by:

Prof. Mark G. Allen, School of ECE

Contributors:

Senior Personnel:

Mark G. Allen, Professor, School of Electrical and Computer Engineering (PD)

Ari Glezer, Professor, School of Mechanical Engineering (co-PD)

Dr. Martin von Arx, School of Electrical and Computer Engineering

Dr. Jeong-Bong Lee, School of Electrical and Computer Engineering

Graduate Students:

Chris Rinehart, Mechanical Engineering

Sung Pil Chang, Electrical Engineering

Brian English, Mechanical Engineering

Submitted to:

Dr. Thomas Beutner

Air Force Office of Scientific Research

This report covers the period August, 1997-September, 2000

TABLE OF CONTENTS

Abstract

In this work, we are investigating the use of microfabrication technology to create a micromachined fluidic control system (consisting of micromachined actuators, sensors, and control/drive circuitry) with a goal of application in practical fluids problems, such as UAV-scale aerodynamic control. Our approaches include: (1) the development of suitable micromachined synthetic jets (*microjets*) as actuators, which obviate the need to physically extend micromachined structures into an external flow; and (2) a non-silicon alternative micromachining fabrication technology based on metallic substrates and lamination (in addition to traditional MEMS technologies) which will allow the realization of larger scale, more robust structures and larger array active areas for fluidic systems.

Introduction

Micromachined devices have been primarily realized using silicon substrates[1]. In many applications, the use of traditional silicon-substrate micromachined devices may be limited, for example by the lack of ability of the surrounding silicon substrate to absorb large mechanical shocks. In this work, we have investigated the use of more robust substrates as suitable starting points for both bulk and surface micromachined structures, as well as investigated the possibility of the substrate forming essential structural components of the device package. Alternative fabrication techniques, such as techniques more commonly used in either conventional machining as well as electronic packaging fabrication (e.g., lamination), are combined with more traditional integrated-circuit-based microelectronics processing techniques to create micromachined devices on these robust substrates.

---

[1] H. Baltes, "CMOS micro electro mechanical systems," *Sensors and Materials*, vol. 9, no. 6, pp.331-346, 1997.

One of the advantages of the use of robust substrates is the possibility of co-fabrication of the micromachined devices and their packages using, e.g., the robust substrate itself as an integral part of the sensor package. Another advantage is that due to substrate robustness, these co-packaged devices may be able to be used in mechanically harsh environments, such as aerodynamic applications. Finally, it is envisioned that the larger-scale devices (especially actuators) producible by this fabrication technology will have increased control authority over their silicon counterparts.

The use of synthetic jets[2] as fluidic actuators enables the possibility of altering the apparent aerodynamic shape of an airfoil by creating a closed recirculation region without extending any mechanical parts into the crossflow of the airfoil. This approach is very suitable for a MEMS-based flow control scheme, since (1) such devices have already been demonstrated as being compatible with micromachining technology[3]; and (2) the relatively 'delicate' MEMS devices do not need to be exposed to the flow; in fact, the devices can be recessed under an orifice plate, safely out of reach of the flow. A microjet, pressure sensor, and provision for integrated circuitry can also be combined together to form a module suitable for repetition into an array. Such a module contains a modulator to switch the synthetic jets on and off at each orifice hole, a pressure sensor to sense the local pressure, and some local electronics to perform readout, signal linearization, and/or local control.

During the project, we addressed the following tasks: (1) development of the fabrication technology for realization of robust micromachined devices; (2) design of pressure sensor arrays and microjet modulator arrays on individual substrates based on these technologies; (3) co-integration of sensors and modulators; (4) improving the sensitivity

---

[2] R. D. James, J. W. Jacob, and A. Glezer, "A round turbulent jet produced by an oscillating diaphragm," *Journal of Physics of Fluids*, vol. 8, no. 9, pp. 2482-2495, 1996.

[3] D. J. Coe, M.G. Allen, M.A. Trautman, and A. Glezer, "Micromachined jets for manipulation of macro flows" in *Proceedings 1994 Solid-State Sensors and Actuators Workshop*, Hilton Head, SC, 1994, pp.243-247.

of the pressure sensors using on-board circuitry, and (5) generation of synthetic jet vortices.

This report summarizes the project period from August 1997 to September 2000, and is divided into three sections: Robust micromachining technology covers the fabrication technology of robust pressure sensors and microjet modulators and their characterization. The section on interface circuitry covers read-out methods for the array of pressure sensors. Synthetic jet technology, finally, covers vortex generation for aerodynamic control using synthetic jets.

1. Robust Micromachining Technology

Robust MEMS-based sensors and actuators were developed in three steps; (i) development of the fabrication technology for the realization of robust micromachined devices; (ii) independent development and optimization of pressure sensors (Section 1.1) and microjet modulators (Section 1.2); and (iii) co-integration of sensors and actuators on the same substrate (Section 1.3).

1.1 Pressure Sensor Development

Two designs of pressure sensor arrays were developed during this project. The first design used stainless steel as a substrate, Kapton film as a pressure-sensitive flexible plate, and electroplated nickel as a back electrode (see appendix). By sensing the capacitance change of the capacitor formed between the flexible diaphragm and the rigid backplate, and by knowing the mechanical properties of the diaphragm, the pressure can be determined. An important attribute of this design is that only the steel substrate and the pressure sensor inlet is exposed to the flow; i.e., the sensor is self-packaged[4]. However, the diaphragm (Kapton) is still exposed to the outside, though somewhat protected by the orifice channel. In some applications it is desirable that only metallic materials are exposed to the outside. Therefore an alternative device was developed that uses a stainless steel diaphragm.

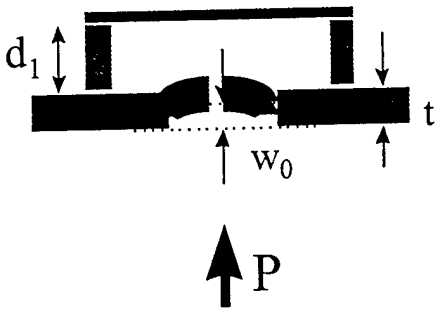

Figure 1.1. Schematic cross-section of the capacitive pressure sensor.

Figure 1.1 shows a schematic cross-section of the device, where d_1 is an initial gap distance between the fixed back electrode and the flexible plate electrode, w_o is the center

---

[4] S.P. Chang, J.B. Lee, and M.G. Allen, "A Robust 8x8 Capacitive Pressure Sensor Array," *proceedings of the 1998 Annual Meeting of the ASME*, 1998.

deflection of the plate, t is the thickness of the plate, and P is the applied uniform pressure. For analytical modeling[5], several assumptions have been made: (1) neglect stretching of the plate; (2) neglect the thickness of the metallic electrode on the plate; (3) neglect residual stress in the plate; and (4) neglect electric field fringing effects. Under these conditions, the capacitance-pressure relationship of the sensor is[4]

$$C_{sensor} = C_0\left(1 + K_1 P + K_2 P^2 + \cdots\right), \tag{1}$$

where K_n are constants given by

$$K_n = \frac{1}{(2n+1)}\left[\frac{a^4}{64Dd_1}\right]^n, \ (n \geq 1), \tag{2}$$

C_0 is the undeflected capacitance, a is the radius of the diaphragm, and D is the flexural rigidity of the diaphragm. The fabrication sequences of the two designs are discussed separately in the following.

Fabrication of Robust Pressure Sensor with Kapton Membrane

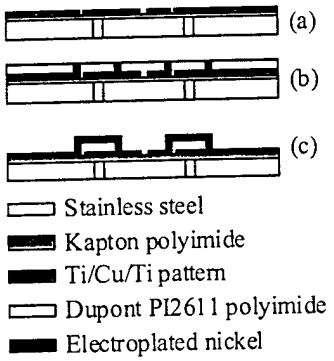

Figure 1.2. Pressure sensor fabrication sequence.

The fabrication sequence of Kapton based pressure sensor array is shown in Figure 1.2. The process starts on square 5.7 cm (2 inch) on a side, 0.5 mm (20 mil.) thick stainless steel substrates. An array of 8x8 pressure inlet holes, with diameters of 2 mm and 5 mm center-to-center distances, are milled through the substrate. Kapton film (DuPont, Kapton HN200, 50μm [2 mil.] thick) is laminated onto the milled substrate using a hot press. This Kapton film will form the pressure sensitive flexible plates in the regions suspended over the milled pressure inlet holes.

---

[5] S. Timoshenko, *Theory of Plates and Shells*, McGraw-Hill Book Company, New York, 1940.

To create bottom electrodes, electroplating seed layers, and bonding pads, a triple metallic layer of Ti/Cu/Ti with thicknesses of 100 Å, 2000 Å, 500 Å, respectively, is deposited and then patterned, shown in Figure 1.2(a). Figure 1.3 (a) shows the metallic layer after patterning. Multiple layers of PI2611 polyimide (Dupont) are then spun onto the patterned layer, and hard-cured in a N_2 ambient at 200 ^{O}C yielding a final thickness of polyimide of approximately 44~48 μm. The polyimide layer is anisotropically etched using a reactive ion etcher(RIE) to create electroplating molds for the support posts of the fixed backplates, and to remove the uppermost titanium layer of the seed layer. The molds are then filled with nickel by electroplating (Figure1.2(b)).

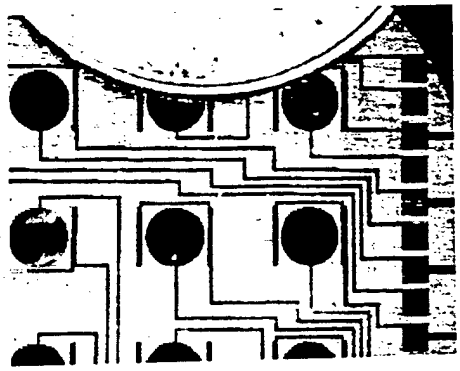

(a)

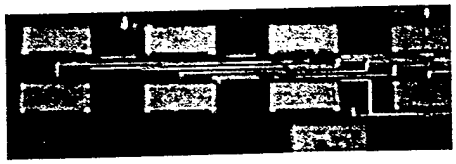

(b)

(c)

Figure 1.3. Photomicrographs of fabricated pressure sensors. (a) diaphragm prior to backplate; (b) backplate view; (c) backplate gap close view

Next, the the backplate is fabricated. A Ti/Cu/Ti metallic triple layer is deposited to form the seed layer for the electroplating step. Thick photoresist (Shipley PR 5740) is spun on the seed layer (approximately 15 μm thick) and patterned to form an electro-plating mold. Then, the mold is filled with nickel by electroplating.

Finally, the thick photoresist and the remaining seed layer are removed. The polyimide sacrificial layers are isotropically etched to release the gap between the fixed backplate and the flexible Kapton polyimide plate (Figures 1.2(c) and 1.3(b,c)). The isotropic dry etch is carried out in a barrel plasma etcher using CF_4/O_2 plasma.

Fabrication of Robust Pressure Sensor with Stainless Steel Diaphragm

The fabrication sequence of the robust pressure sensor with stainless steel diaphragm starts on the same substrate as the Kapton type sensor, followed by lamination of Kapton as discussed above. Next, a stainless steel film is laminated. Reactive ion etcher is used to remove the Kapton under the stainless steel membrane through the pressure inlet holes. This membrane forms the flexible plates in the regions suspended over the milled pressure inlet holes. Then, for an insulation layer an Su-8 2 Epoxy layer is deposited with a thickness of 3μm.

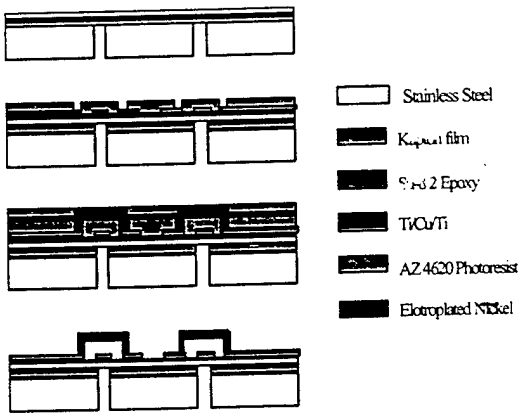

Figure 1.4: Fabrication sequence of pressure sensor based on stainless steel membrane.

To create bottom electrodes, electroplating seed layers, and bonding pads (Figure 1.4), a triple metallic layer of Ti/Cu/Ti is deposited with a thickness of 250/6000/250 Å and patterned. Two layers of AZ4620 photoresist are spun onto the patterned layer, yielding a final thickness of photoresist of approximately 50~55 μm. The photoresist is patterned to create electroplating molds and nickel supports are electroplated through the molds.

To fabricate the backplate, a seed layer of Ti/Cu/Ti is deposited. Thick photoresist (AZ 4620) is spun on the seed layer (approximately 20μm thick) and patterned to form electroplating molds. These molds are then filled with Nickel by electroplating.

Finally, the photoresist sacrificial layers and the seed layers in between them are etched to release the gap between the fixed backplate and the pressure sensitive stainless steel diaphragm. Figure 1.5 shows a photomicrograph of the patterned sensor array.

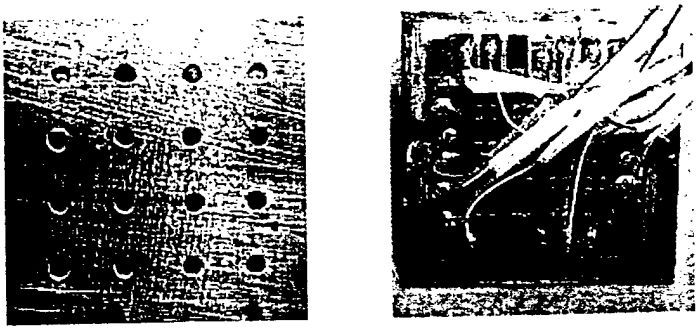

(a) (b)

Figure 1.5. Photomicrographs of fabricated pressure sensors. (a) side exposed to flow. (b) sensor view.

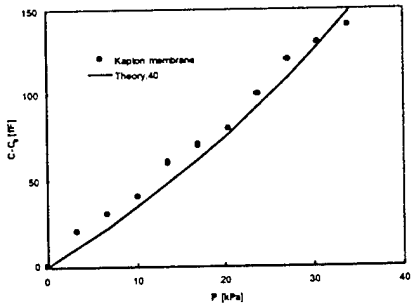

Figure 1.6. Net capacitance change versus pressure for Kapton membrane pressure sensor.

Characterization of Pressure Sensors

The capacitance of individual pressure sensors has been measured using a Keithley 3322 LCZ meter. First we show data obtained with Kapton membrane sensors. Measured capacitances for undeflected pressure sensors were in the range from 11.35 pF to 13.97

pF depending on the length of interconnections between bonding pads and sensors. Over an applied pressure range from 0 to 34 kPa, the net capacitance change was approximately 0.14 pF. This corresponds to an average absolute sensitivity of 4.1 fF kPa^{-1} or an average relative sensitivity of 295×10^{-6} kPa^{-1}. Theoretical prediction of the sensor behavior is determined by taking the first three terms of equation (1) (i.e., up to n=2). The theoretical data shown in Figure 1.6 is based on an initial gap (d_1) of 40 μm. There is approximately a 10~20 % difference between the measured physical gap and the 40 μm gap value used to provide a best fit between theory and experiment. This difference could be explained by the fringing effects of the sensor capacitance. The measured values of relative capacitance change are in the range from 1% to 1.34 %.

Measurement data of the stainless steel membrane pressure sensor is shown in Figure 1.7. The capacity at zero pressure ranged between 59 pF and 95 pF for different devices. In Figure 1.7, this value is 69.35 pF. The sensitivity is much smaller than the Kapton-membrane-based pressure sensor due in part to the higher modulus of elasticity of stainless steel. The measured sensitivity is 1.98 fF kPa^{-1}.

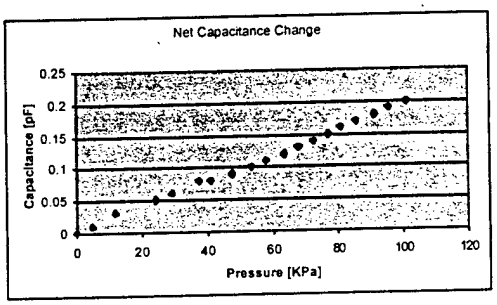

Figure 1.7: Capacitance versus pressure for stainless steel membrane pressure sensor

1.2 Microjet Modulator Development

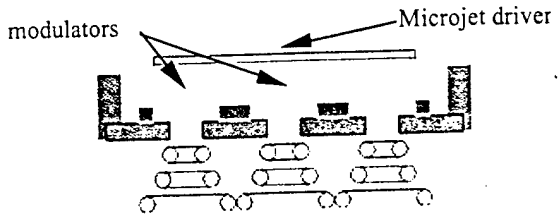

Figure 1.8. Creation of synthetic jets using an array of modulators with one microjet driver.

The purpose of the microjet modulator is to enable the possibility of altering the apparent aerodynamic shape of an airfoil by creating a closed recirculation region without extending any mechanical parts into the crossflow of the airfoil. The modulation concept pursued in this project is shown in Figure 1.8. A micromachined array of modulators is assembled with one piezoelectric microjet driver. The driver compresses the air on the rear-side of the modulators. The modulators control the magnitude and phase of the airflow through their orifices. By controlling the timing of the modulators, various synthetic jet profiles are formed with centerline velocities of the order of 3 m/s.

By incorporating conventional machining technology with lamination and surface micromachining, robust actuators were achieved, and synthetic jets were generated. Two different actuation schemes were investigated: electrostatic actuation and thermoelectric actuation. Fabrication and characterization of these devices are discussed in the following subsections. The synthetic jets were characterized using particle image velocimetry (PIV).

Electrostatically actuated Microjet Modulators

Figure 1.9 shows the actuator concept being pursued for electrostatic actuation. Sheets of material are laminated onto a stainless steel substrate, lithographically patterned, and surface micromachined to form standoffs and flow channels. The flow channels permit airflow through an orifice conventionally machined in the substrate when the actuators are in the 'off' position. When the actuators are energized by application of a voltage between the flexible sheet and the substrate, the

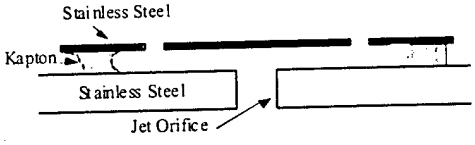

Figure 1.9. Schematic cross-section of electrostatically actuated microjet modulator.

flexible sheet is deflected toward the surface, constricting the airflow and ultimately blocking the orifice.

The process (Fig. 1.10) begins with a 0.05 inch milled stainless steel substrate, Kapton polyimide film, and 12.5 μm SS 302 foil. The milled substrate is 2" x 2" with 25 milled holes 2 mm in diameter. The Kapton is Type 200 HN from DuPont, and the SS302 thin film is a prefabricated, over-the-counter shim stock.

To fabricate the actuators, the Kapton is first laminated to the milled substrate, and the SS foil is laminated to the Kapton. This is done in two steps for improved adhesion between each layer. Next, photolithography is used to mask the stainless steel sheet for wet etching. The stainless steel is formed into three different types of actuator geometries using a wet etch. Finally, the Kapton is removed using an isotropic dry etch, in which the stainless steel film serves as the mask for surface micromachining of the underlying Kapton. Since large areas of stainless steel are not underetched completely, the remaining Kapton serves as anchor of the structure.

A photograph of a two inch substrate bearing stainless steel modulators is shown in Figure 1.11. Some of the modulators have been removed to show the underlying orifice holes. At the center device, the shaped stainless steel has been removed to show the underlying Kapton film.

We tested six geometries, shown in Figure 1.12. The outer ring is the support ring. It anchors the device to the substrate. To provide a reliable anchor, its size is chosen large compared to the under-etching distance of Kapton.

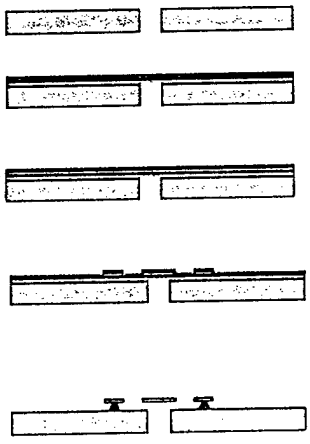

Figure 1.10. Fabrication sequence of electrostatically actuated modulator array.

The first three geometries use a homogeneous concentric circle as support ring. A minimum size of 1 mm is required to get a reliable anchor. The devices have therefore a large total size of 10 mm. To reduce this size, the shape of the support ring was modified in versions (d)-(f). Only part of the outer circle is used as an anchor. The rest of its area can then be used for the springs and the overall size is reduced while retaining the spring length.

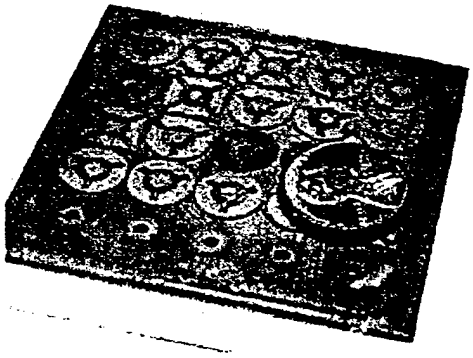

Figure 1.11. Photograph of an electrostatically actuated modulator array.

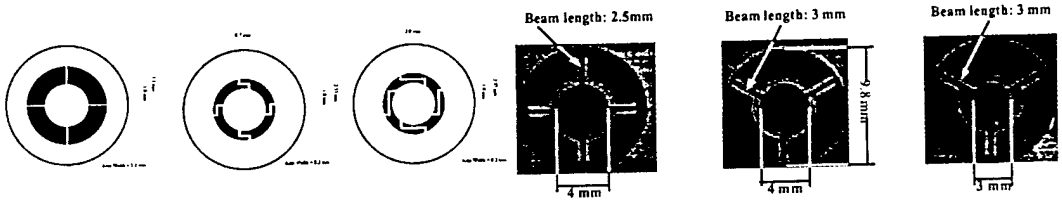

(a) (b) (c) (d) (e) (f)

Figure 1.12 Various device shapes were designed to optimize the modulator performance.

Verification of operation using PIV

Particle image velocimetry (PIV) tests were performed on the modulator actuators, both to demonstrate that synthetic jet flow could pass through the modulators, as well as to demonstrate modulator-based control of the synthetic jet flow. Both a single modulator test (in which one isolated modulator was turned 'on'), and a dual modulator test (in which one of two adjacent modulators was turned 'on') were performed.

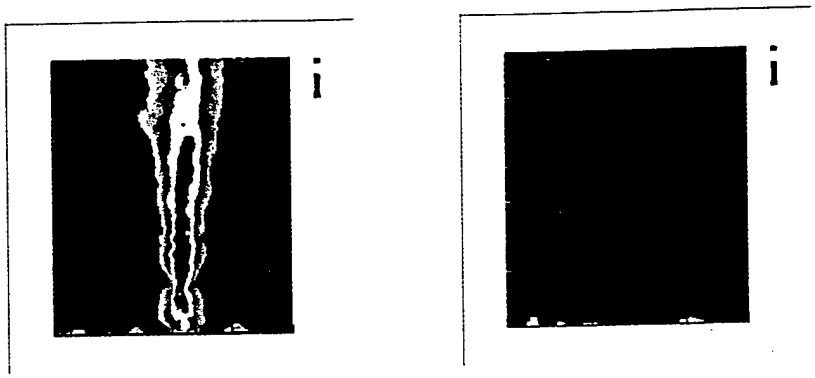

(a) (b)

Figure 1.12. Velocity magnitude plot for single and dual modulator test using PIV.

For the single valve PIV test, the modulator type c (2.75 mm total length) described above was used, and the piezo-driver was driven at 900 kHz. Figure 1.13 shows the velocity magnitude plot for this test. Before electrostatic actuation (i.e., before the pad was drawn down to cover the orifice hole) the centerline velocity from the orifice was measured at 3 m/s, Figure 1.12 (a). Once actuated the centerline velocity is ~0 m/s, Figure 1.12 (b). This experiment demonstrates that the modulator can physically stop a flow by controlled actuation.

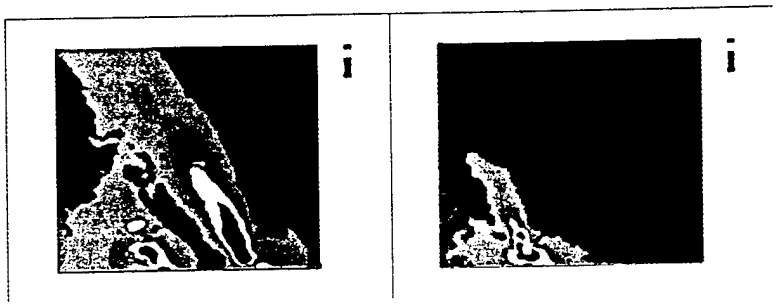

(a) (b)

Figure 1.13 Velocity magnitude plot of dual valve PIV test. (a) Both valves open. (b) Only left valve open.

The dual valve PIV tested the change in the velocity magnitude plot, when one valve was constantly open and the other valve was modulated. This test used the modulator shown in Figure 1.12 (b) with a spring length of 1.4mm. Again, centerline velocities of ~3 m/s

were measured when both valves were open (Fig. 1.13 (a)). When one valve was actuated, the centerline velocity through the other hole remained constant. (Fig 1.13 (b)).

In attempts to reduce actuation voltages and achieve significant process yields, combinations of various geometrical parameters have been tested. The following parameters were varied: beam length, gap size, actuator disc diameter d_a, and orifice diameter d_o. The yield and the pull down voltage of each device was measured.

To increase the electrostatic force, the effective area of the capacitor, i.e. the overlap between substrate and diaphragm can be increased. The effective capacitor area is $A_{eff} = \pi(d_a^2 - d_o^2)/4$. To increase A_{eff}, the size of the orifice was reduced. However, with a 1mm orifice, the fabrication yield deceased to 15-20% with most losses at the edge of the substrate. These losses may be attributed to higher reactive ion gas concentrations at the edges of the substrate that lead to faster etching rates. The 1mm orifice devices

Device #	# Beams	Deflection Distance um	Effective Area sq.mm	Beam Width um	Beam Length um	Average Voltage V	Experimental Voltages V	# Tested
1	3	25.4	9.425	400	3000	150	150-150	2
2	3	25.4	9.425	400	2500	190	150-230	2
3	3	25.4	9.425	400	2000	400	440-360	2
4	3	25.4	3.927	400	3000	260	260,000	2
5	3	25.4	3.927	400	2500	165	150-180	2
6	4	25.4	9.425	400	3000	150	150	2
7	4	25.4	9.425	400	2500	325	300-350	2
8	4	25.4	9.425	400	2000	230	230	1
9	4	25.4	9.425	600	3000	203	155-250	2
10	4	25.4	9.425	600	2500	310	270-350	2
11	4	50.8	3.927	400	2500	165	150-180	2
12	4	50.8	3.927	400	2000	280	160-400	2
13	4	50.8	3.927	600	3000	350	300-400	2

Table 1.1: Pull down voltages of microjet modulators for various sizes

repeatedly exhibited pull down voltages under 200 V. However, the centerline flow velocity was reduced to approximately 1 m/s. Previous testing has produced jets with centerline flow velocity of approximately 3 m/s. Table 1.1 shows pull down voltages obtained with various device geometries.

We conclude that the actuation voltage of the electrostatically actuated modulators can be reduced below 200 V. Significant reduction of the voltage, however, can not be achieved without reducing the flow velocity of the air jet. To achieve better performance we will investigate a different actuation scheme in the next section.

Thermoelectrically actuated Microjet Modulators

Figure 1.14 shows the actuator concept for thermoelectrically actuated microjet modulators. A U-shaped cantilever of a bimorph material is attached to the substrate with two support arms. The valve plate covers the orifice hole initially, therefore restricting the airflow through the orifice. By applying a current through the two support arms, the cantilever is heated. Because of the small width of the arms compared to the valve plate, most of the resistance appears in the arms. Consequently, most of the heat is dissipated there. The bimorph arms are bent and the valve plate is displaced, therefore enabling airflow through the orifice.

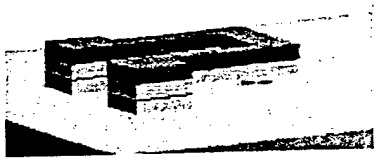

Figure 1.14. Schematic of thermo-electrically actuated microjet modulator.

The fabrication sequence, shown in Figure 1.15, starts with the same stainless steel substrate as discussed above. An aluminum sheet is then laminated using epoxy as adhesive. This will form the sacrificial layer. Next, the bimorph material is fabricated. Copper and titanium are laminated using the same adhesive mentioned above. To pattern the top layer titanium, photoresist is deposited and patterned, and the titanium is etched using 10% HF. The exposed adhesive between titanium and copper is then removed in a barrel etcher for 45 min. The copper is etched using NH_3OH saturated with copper-sulfate, and exposed epoxy is removed from the aluminum surface.

To release the structure, the aluminum is etched isotropically using KOH. Figure 1.16 shows a photograph of a thermoelectrically actuated microjet modulator array.

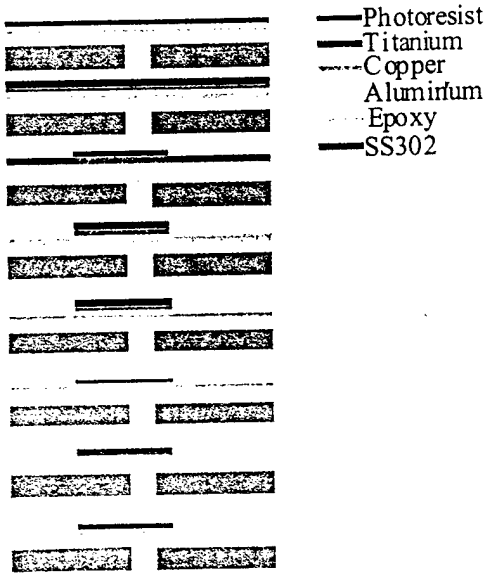

Figure 1.15. Fabrication sequence for thermoelectrically actuated microjet modulator.

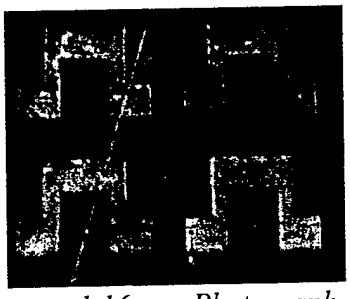

Figure 1.16 Photograph of thermoelectrically actuated microjet modulator array.

1.3 Co-Fabrication of Sensors and Actuators

The last two sections covered the development of pressure sensors and microjet modulators, fabricated independently. This section covers the co-fabrication of robust modulators and pressure sensors on the same stainless steel substrate. A schematic of the sensor and actuator system is shown in Figure 1.17.

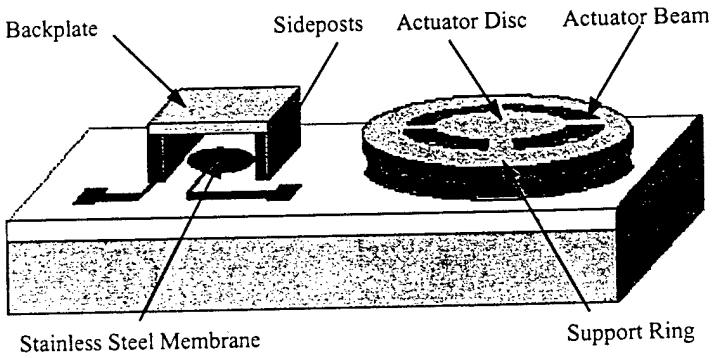

Figure 1.17: System of robust pressure sensor (L) and microjet modulator (R)

The sensor contains a stainless steel membrane, which is exposed to the outside through a pressure inlet hole. When pressure is applied to the membrane, it deflects toward the fixed back plate. The distance between the bottom electrode and the fixed electrode decreases and the capacitance increases.

The right hand side of Figure 1.17 shows the actuator concept being pursued. Sheets of material are laminated onto a stainless steel substrate, lithographically patterned, and surface micromachined to form standoffs and flow channels. The flow channels permit airflow through an orifice conventionally machined in the substrate when the actuators are in the 'off' position. When the actuators are energized, the flexible sheet is deflected toward the surface, constricting the airflow and ultimately blocking the orifice. For this demonstration, the actuators are driven electrostatically, by application of a voltage between the flexible sheet and the substrate.

Co-Fabrication of Sensor and Actuator

The co-fabrication sequence of robust pressure sensors and robust modulators starts on a square stainless steel substrate with a side length and thickness of 60mm (2.4 inches) and 0.9 mm (36 mil), respectively. Pressure inlet and jet holes with diameters of 2mm are

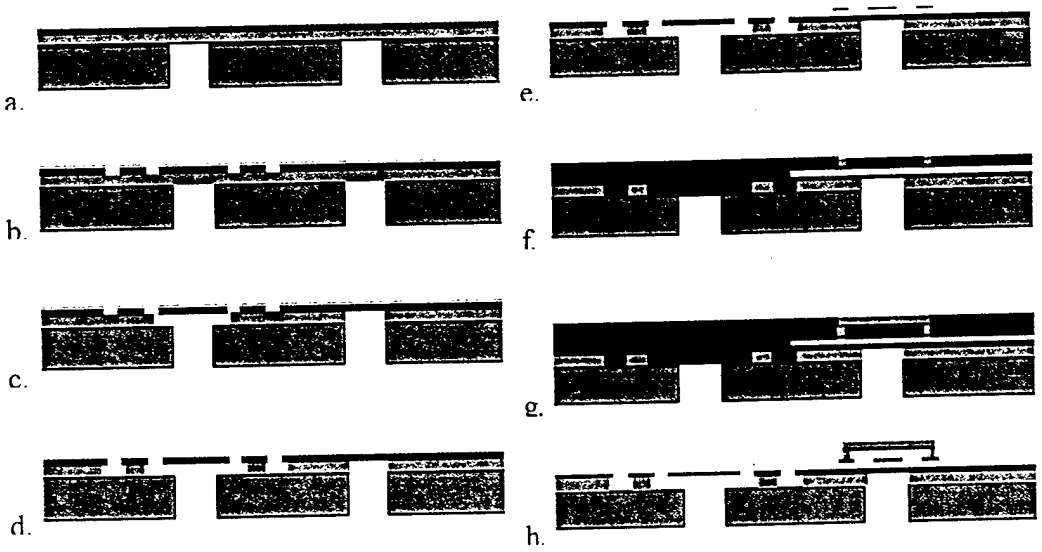

Figure 1.18: Fabrication sequence for sensors and actuators

milled through the stainless steel substrate. Figure 1.18 shows the fabrication sequence in greater detail.

A 50μm thick Kapton HN 200 polyimide film and 12.5μm stainless steel film are laminated on the milled stainless steel substrate using a hot press (Fig. 1.8 (a)). To form the actuator disc, the support ring, and the actuator beam polyimide 2611 is spin coated on the surface of the stainless steel film, cured and patterned. Then the stainless steel film is etched (Fig. 1.18 (b)).

Next, the Kapton film under the stainless steel film is dry-etched through the backside holes of the sensors and actuators. The Kapton under the suspensions of the actuator plates is etched from the front side. The holes for the sensors are sealed with polyimide tape, and the etching of the Kapton film under the actuators is continued to release the actuators (Figs. 1.18 (c, d)).

Then the bonding pads, interconnection lines and bottom electrodes, and the seed-layers for the electroplating steps are formed. Ti/Cu/Ti (30/600/30 nm) is deposited and patterned, (Fig. 1.18 (e)). Positive photoresist AZ 4620 forms the molds of the side posts of the sensor. Finally, NiFe is electroplated through the mold (Fig. 1.18 (f)).

To fabricate the back plate of the sensor, a seed-layer is deposited and patterned. AZ4620 positive photoresist defines a mold. Then NiFe is electroplated, (Fig. 1.18 (g)). Finally the two photoresist layers, and the second seed layer are removed, (Fig. 1.18 (h)).

The final system of sensors and actuators is shown in Figure 1.19.

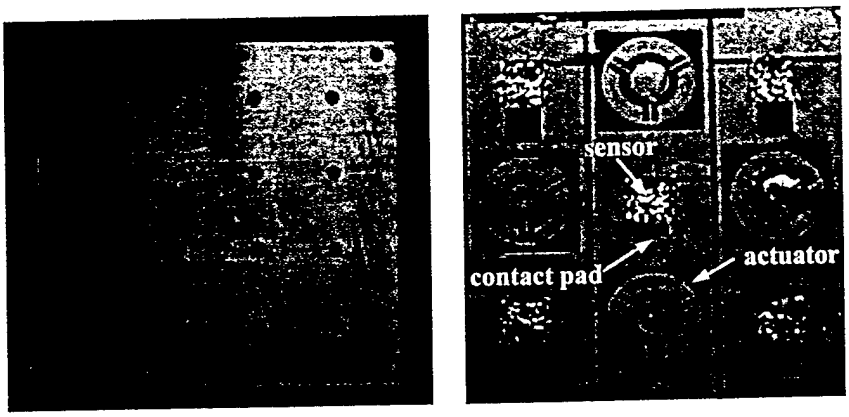

Figure 1.19. Photomicrographs of fabricated sensors and actuators

Characterization of Co-Fabricated Sensor and Actuator

The capacitance of the pressure sensors has been measured using a Keithley 3322 LCZ meter. Measured capacitances for undeflected pressure sensors were in the range of 73.4 pF to 93.5 pF. A large fraction of these values originates from parasitic capacities of the connection lines and bonding pads on the substrate. The capacitance change is shown in the Figure 1.20 as a function of applied pressure.

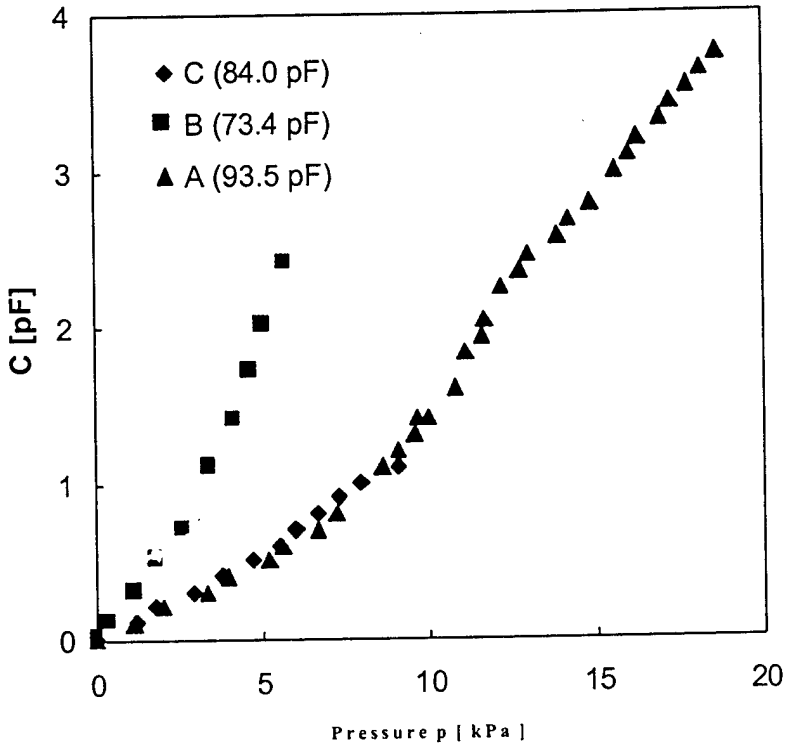

Figure 1.20: Capacitance of three devices as a function of applied pressure.

2 Interface Circuitry

The capacitance values of the pressure sensors are easily measurable with state of the art capacitance meters. However, the sensitivity of these measurements are limited by parasitics. While stray capacitances can be reduced by design, the connection wires to a remote measurement site increase noise and therfore reduce the sensitivity. While this can be compensated in part by averaging, this approach is not applicable for a real time application with a bandwidth of 1 kHz. Such a bandwidth is needed to resolve aerodynamic fluctuations of the pressure. Furthermore, an array of devices should be accessible through a reasonable number of signal lines. These arguments demonstrate the need for on-board read-out circuitry for the pressure sensor. Both discrete and ASIC design approaches were therefore developed to measure the stray sensitive capacitance values.

The modulators in this project are based on electrostatic and thermal actuation. Both types are easily driven by external equipment. Therefore, we did not integrate any control logic for the actuators into the different versions of circuits discussed here.

A first read-out circuit is discussed in Section 2.1. An oscillator was built using discrete components. Its resonance frequency depends on the capacitance of the pressure sensor. This is used to measure the pressure. This scheme is accurate if the integration time of the frequency counter is larger than 1s. The scheme is not feasible to resolve aerodynamic pressure fluctuations. Furthermore, only one sensor can be interfaced with the circuit.

The second device addresses all limitations of an off-board measurement approach. An ASIC chip interfaces to four sensors. Its output voltage is proportional to the capacitor difference of the selected sensor and an on-chip reference. The device is discussed in Section 2.2.

2.1 Discrete Circuits for a single pressure sensor

Figure 2.1 shows data of a pressure sensor with stainless steel membrane. It was obtained with a circuit based on a operational amplifier LF356 in a DIP8 package and 160kΩ resistors. The output frequency f is shown as a function of the pressure p. The sensitivity of the pressure sensor system is typically -168×10^{-6} kPa^{-1} for sensors based on a stainless steel membrane.

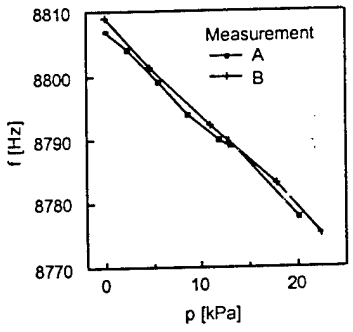

Figure 2.1: Output frequency as a function of pressure for a sensor with stainless steel membrane.

2.2 Analog ASIC Design for multiple pressure sensors

A simplified schematic of the ASIC is shown in Figure 2.2. One of four sensors can be selected with on-chip switches. The chip uses a standard switched capacitor (SC) architecture to measure the difference between the capacitance of the selected sensor and an on-chip reference. The transfer function from the sensor capacitance C_{sensor} to the output voltage V_{out} is the following

$$V_{out} - V_{cm} = -5(V_{sig} - V_{icm})\frac{C_{sensor} - C_{ref}}{C_{ref}} + 5(V_{ref} - V_{sig}),$$

where the reference capacitance C_{ref} can be adjusted between 10pF and 70pF in seven steps to compensate for the process dependent sensor capacitance at zero pressure. It can be further tuned by the voltage V_{ref}-V_{sig}. The voltage V_{sig}-V_{icm} determines the sensitivity.

The operational amplifier is based on a standard folded cascode architecture. At a bias current of 40 µA the op-amp dc power consumption is 1.2mW. The open loop gain is 62dB and the gain bandwidth product is 11.9MHz with a phase margin of 59° for a load capacitance of 5pF. The first and second poles are at 12kHz and 32MHz, respectively. With a SC feedback gain of 5 a gain inaccuracy of 0.4% is achieved when switch noise is

neglected. For $C_{sensor} = C_{ref} = 70pF$ the bandwidth is 394kHz. These data were obtained with HSpice using a netlist that was exported from CADENCE.

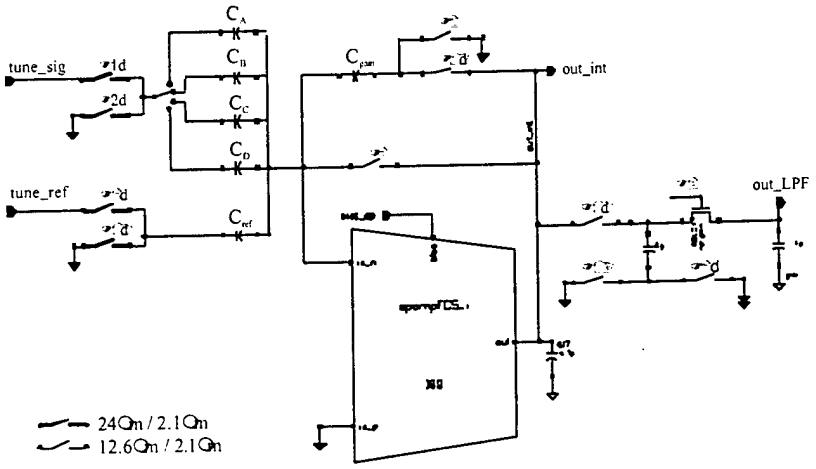

Figure 2.2: SC amplifier to measure the sensor capacitances C_A, C_B, C_C, C_D.

clock feed through. Two different sizes of switches were chosen, to optimize speed versus clock feed through.

The amplifier was integrated with additional circuitry for clock generation, bias generation, buffering the output and on-chip trimming. To achieve reasonable settling, a clock speed of 50 kHz was chosen. The layout was drawn with the ASIC design software CADENCE and fabricated on a MOSIS ABN 1.5µm run. This process supports linear poly-poly capacitors and has two metal layers. The total core area is 2.3 mm^2. The size of the chip including the 40 pads is 2.2 mm × 2.2 mm.

The ASIC was characterized using a standard capacitor of 49pF instead of the sensor, a supply voltage of 4.993V, and control voltages V_{cm} and V_{sig} of 2.995V and 2.492V, respectively. Figure 2.3 (a) shows the output waveform before the low pass filter stage. The time constant of the system is 0.29 µs.

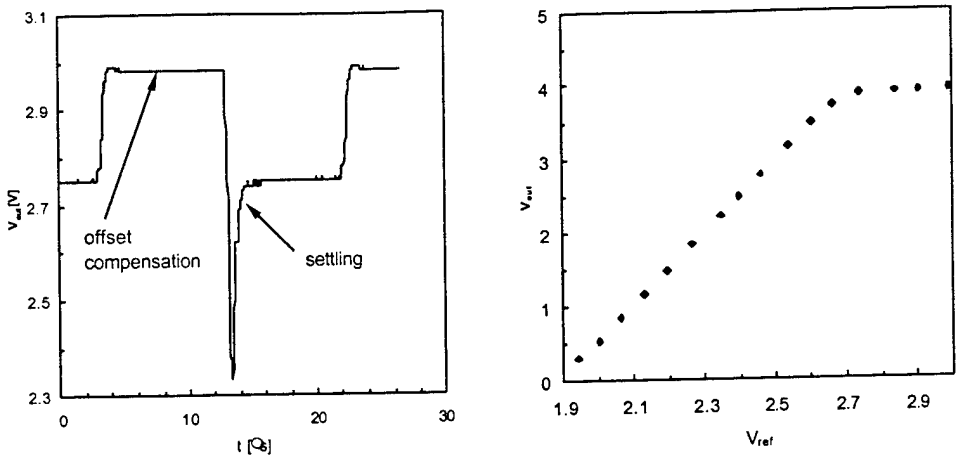

Figure 2.3. (a) Output waveform when the sample and hold (low pass filter) is disabled. (b) Output voltage versus V_{ref} to test the gain.

When the on-chip low pass filter (LPF) is enabled, the waveform is sampled at the end of the settling time, and V_{out} can be measured. To test the voltage gain, the voltage V_{ref} was varied. Figure 2.3 (b) shows V_{out} versus V_{ref}. The gain of V_{out} versus V_{ref} is 4.89 to be compared with 5.0 for ideal on-chip capacitor ratios and infinite op-amp gain. Finally, the ASIC was connected to two pressure sensors based on stainless steel diaphragms. Figure 2.4 shows the output voltage versus pressure. For this measurement V_{dd} was 5.0 V, V_{cm} = 2.675 V, V_{sig} = 0 V, and V_{ref} was 0.420 V for sensor B. The sensitivity using the ASIC is 844 μV kPa^{-1} and 496 μV kPa^{-1} for the two sensors, respectively.

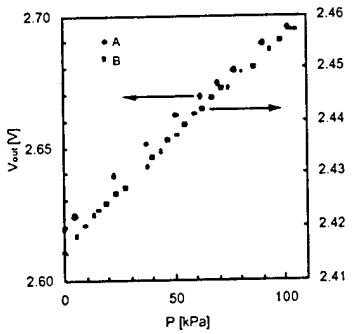

Figure 2.4. Output voltage of the ASIC versus pressure for a sensor with a stainless steel diaphragm.

3. On-demand Synthetic Jet Vortex Generation

Vortex generators of varying scales are widely utilized in numerous aerodynamic applications to prevent or delay flow separation by inducing the formation of streamwise vortices of a prescribed sign near the flow surface. In current realizations, vortex generators are typically made of spanwise rows of passive plates that are permanently mounted on the flow surface and thus affect the flow and contribute to the aerodynamic drag even in the absence of separation. Compton and Johnston proposed in 1992 to emulate the effect of a vortex generator by using a jet that issues normal to the surface which has the advantage that it can be "removed" when not needed simply by turning the jets off. Pitching or skewing of the jet relative to the oncoming flow leads to the evolution of a *single sign* streamwise vortex where the sense of the rotation is determined by the skew direction and vortex strength is determined by the skew angle. However, with a fixed nozzle, this vortex generator is limited to a fixed sign vortex.

This part of the project focuses on the development of batch-fabricated arrays of fluidic-based vortex generators that are capable of generating streamwise vortices having prescribed sign and strength. Each element in the array is comprised of a pair of adjacent rectangular synthetic (zero net mass flux) jets where the jet spacing (along their long dimensions) is comparable to the width of the jet orifice. Each jet can be produced over a broad range of scales by an actuator comprised of a closed chamber having an orifice and an oscillating diaphragm that is built into one of the chamber walls. Earlier work (Smith and Glezer[6]) has shown that when the jets are operated in concert in this configuration, the combined jet can be vectored towards one of the jets by advancing the phase of the actuation signal of that jet. Thus, when the jet pair is placed in a cross flow, and is skewed in the spanwise direction, it evolves into a single-sign streamwise vortex. The direction and degree of spanwise vectoring (and thus the sense of rotation and the

---

[6] B. L. Smith and A. Glezer, "The formation and evolution of synthetic jets," *Phys. Fluids*, **10**, 1998, pp. 2281-2297.

strength of the ensuing streamwise vortex, respectively) can be controlled by varying the sign and magnitude of the phase difference between the driving signals.

The interactions between arrays of synthetic jet pairs and a cross flow of varying speed is investigated in a small-scale closed-return wind tunnel having a square test section that measures 15 cm on each side and a maximum speed of 13 m/s. The test section is specifically designed to enable particle image velocimetry in the cross-stream (x-y) and spanwise (y-z) planes. Arrays of jet pairs having a common dividing partition are fabricated using lithographic techniques and are integrated into the test section wall. The jets are driven using piezoelectric membranes. Each orifice is 0.5 mm wide, and 25 mm long, and the jet pairs are spaced 14 mm apart on center. In the present experiments, the driving frequency is 980 Hz, and jet Reynolds number (Smith and Glezer[2]) is 200.

The flow field of a single jet pair in the absence of a cross flow is shown in two orthogonal planes across and along the jet pair centerline in Figures 3.1a and b, respectively. The data in Figure 3.1a shows that a single jet is formed within two orifice widths off the surface, and begins to spread rapidly around $y/c \approx 0.3$ (c is the length of the orifice). The formation of successive vortex pairs is apparent downstream of the orifice. The image also shows the formation of wall boundary layers on the surface on either side of the jet orifice as a result of the suction that is associated with the formation of the jet. In the orthogonal view (along the jet pair centerline, Figure 3.1b), the combined jet

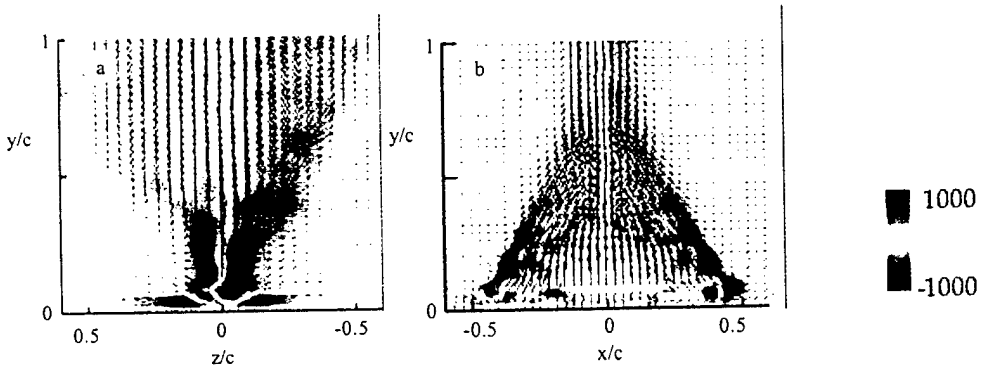

Figure 3.1 (a) Spanwise view of jet-pair in absence of cross flow. (b) Streamwise view of jet-pair in absence of cross flow.

narrows rapidly through y/c ≈ 0.7, where its width appears to be invariant with streamwise distance. These images suggest that similar to conventional rectangular jets, the synthetic jet undergoes axis switching which is ostensibly associated with the evolution of the rectangular vortices that form at the jet orifice (note the discrete vortices near the edges of the jet).

The jets are placed in the cross-flow so that their axes are aligned with the streamwise direction. As the velocity ratio between the jet and the cross flow VR is decreased, the jet bends in the streamwise direction and its penetration distance into the cross flow decreases. Figure 3.2 is a composite of three streamwise stations for VR=0.8 (a) and 0.48 (b). While the penetration height of the jet into the cross flow decreases, the vorticity concentrations that originate from the downstream edge of the jet orifice persist through the downstream edge of the measurement domain. These successive concentrations are advected at the speed of the free stream, and the spacing between them increases with decreasing velocity ratio (the jet frequency is invariant).

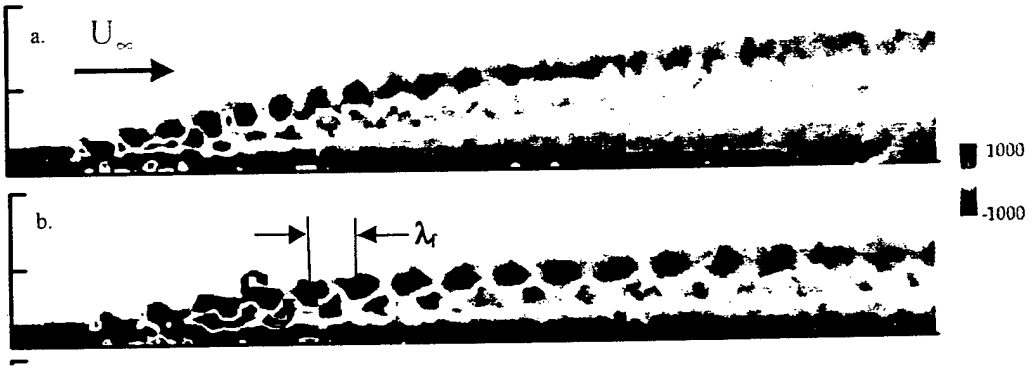

Figure 3.2. Jet penetration into cross flow, VR = 0.8 (a), 0.48 (c).

The penetration depth is characterized by the cross-stream height of the center of rotation of the cross-stream velocity distribution that is induced by the CW vortices. (Figure 3.3a). The height of this center y_d (shown schematically in Figure 3.3a) is chosen as a measure of the penetration depth. Figure 3.3b shows the streamwise variation of the penetration depth for a number of velocity ratios. It is remarkable that for VR ≥ 1.2, the

slope of these plots in the far-field is relatively invariant regardless of the the velocity ratio.

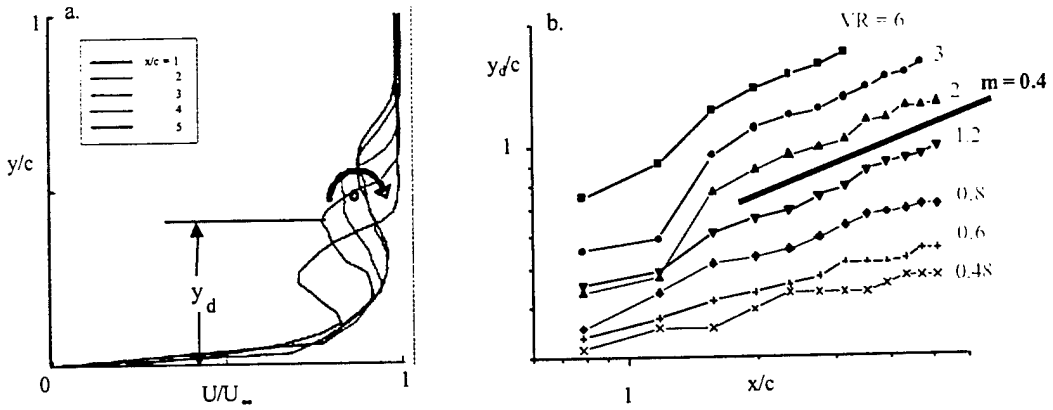

Figure 3.3. Jet penetration (a) Streamwise velocity profiles at VR = 0.8, (b) Penetration depth vs. downstream distance for various VR's

The evolution of the ensuing streamwise vortices in the cross-stream y-z plane (looking in the streamwise direction) is shown in Figures 3.4a-d for x/c = 1 (Figures 3.4a and b) and x/c = 2 (Figures 3.4c and d). When the two jets in the pair are in phase, symmetric counter-rotating vortex pairs much like those of conventional jets are present (Figure 3.4a). Farther downstream the counter rotating vortices lift off the surface and a pair of secondary streamwise vortices is induced near the wall (in the wake of the primary jet). Horizontal velocity distributions through the cores of the primary vortices show strong upwash in the center plane of the two vortices. Vectoring the jet pair using an imposed phase difference of 150° between the jet pair (Figure 3.4c and d), leads to the formation of a strong single-sign CCW vortex as well as a weaker opposite sign vortex. This pattern persists in the streamwise direction and the formation of the opposite sense secondary vortices is apparently suppressed while the (primary) vortex core remains at nearly the same elevation.

Figures 3.5a and b show vorticity distributions in the cross-stream (y-z) plane for in-phase and out of phase ($\Phi = 150^0$) jets pairs within an array of 5 jets. When all jets are in phase, the vortex pair grows and moves away from the surface. However when the

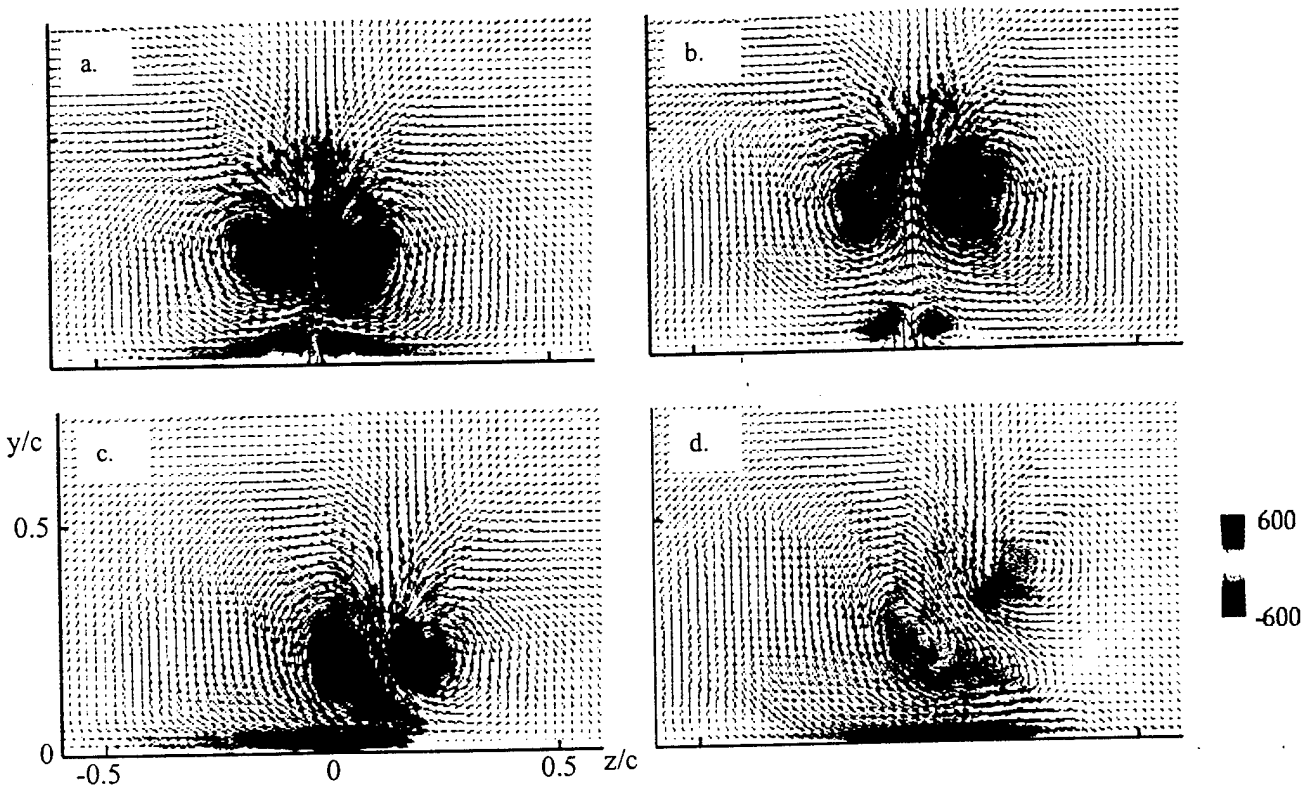

Figure 3.4 Cross stream vorticity contour maps for VR = 0.8 (a) $\Phi = 0^o$, x/c = 1, (b) $\Phi = 0^o$, x/c = 2 (c) $\Phi = 150^o$, x/c = 1 (d) $\Phi = 150^o$, x/c = 2.

phase between the jets is nonzero, the vortex core of the dominant vortex remains at about the same height while the vortex itself stretches. The weaker opposite sense vortices rotate slightly around the dominant vortex and continue to weaken with downstream distance. These data demonstrates that it is possible to engender a spanwise array of same sign vortices as shown in Figure 3.5b.

In conclusion, single-sign streamwise vortices are formed by spanwise vectoring of a pair of rectangular synthetic jets issuing into a cross-flow thus providing on-demand vortex generation without alteration of surface geometry. In the absence of the cross-flow, the jet pair merges into a single jet, and the merged jet undergoes strong axis switching. The penetration height of the unforced jet into the cross flow varies as $x^{0.4}$ and decreases with the velocity ratio. The spanwise vorticity of the jet is modulated at the formation frequency. The merged jet is vectored by simply varying the relative phase of

the jet pair driving signals and the sense (i.e. CW or CCW) and strength of the streamwise vortex is controlled by the direction and magnitude of the jet vectoring angle.

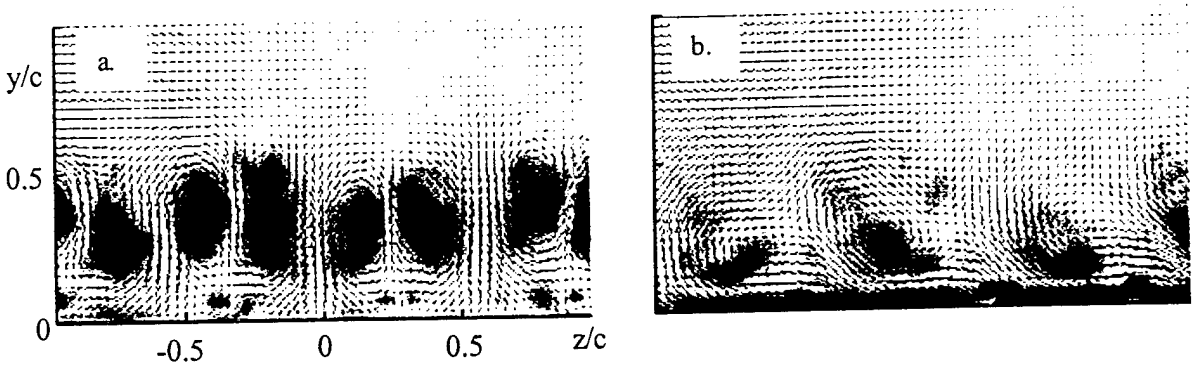

Figure 3.5. Cross stream vorticity contour maps of a jet array for VR = 0.8 , x/c = 3 (a) $\Phi = 0^o$ (b) $\Phi = 150^o$.

4. Conclusions

Robust materials have been studied as suitable substrates for micromachined devices. Lamination combined with traditional micromachining processes has been investigated as a suitable fabrication process for the robust substrates.

A robust modulator array using a robust stainless steel shim stock, Kapton film as an insulator, stainless steel metal foil as a modulator body has been designed, fabricated, and characterized. The PIV tests for parts of robust modulator arrays show that microjets of the order of 3 ms^{-1} can be modulated using this device.

A capacitive pressure sensor array using a robust stainless steel shim stock, stainless steel diaphragm, and lamination processing has been designed, fabricated, and characterized. Two types of devices were developed. The first one is based on a Kapton diaphragm. It has a high sensitivity of 4.1 $fFkPa^{-1}$. The second type utilizes a stainless-steel membrane. This robust design has the drawback of a smaller sensitivity of 1.98 $fFkPa^{-1}$.

Read-out circuitry has been designed and integrated with the pressure sensors. The first approach uses discrete circuits, providing a frequency-modulated output. The second approach is an ASIC chip designed to interface to an array of four sensors.

5. Acknowledgement/Disclaimer

This work was sponsored in part by the Air Force Office of Scientific Research, USAF, under grant/contract number F49620-97-1-0519. The views and conclusions contained herein are those of the authors and should not be interpreted as necessarily representing the official policies or endorsements, either expressed or implied, of the Air Force Office of Scientific Research or the U.S. Government.

Appendices

Previously-provided interim reports are appended to this final report

DEMONSTRATION OF ROBUST MICROMACHINED JET TECHNOLOGY AND ITS APPLICATION TO REALISTIC FLOW CONTROL PROBLEMS

AFOSR GRANT F49620-97-1-0519

Mark G. Allen and Ari Glezer
School of Electrical and Computer Engineering &
School of Mechanical Engineering,
Georgia Institute of Technology, Atlanta, GA

Abstract

In this work, we are investigating the use of microfabrication technology to create a micromachined fluidic control system (consisting of micromachined actuators, sensors, and control/drive circuitry) with a goal of application in practical fluids problems, such as UAV-scale aerodynamic control. Our approaches include: (1) the development of suitable micromachined synthetic jets (*microjets*) as actuators, which obviate the need to physically extend micromachined structures into an external flow; and (2) a non-silicon alternative micromachining fabrication technology based on metallic substrates and lamination (in addition to traditional MEMS technologies) which will allow the realization of larger scale, more robust structures and larger array active areas for fluidic systems. As an initial study, an array of MEMS pressure sensors and an array of MEMS modulators for orifice-based control of microjets have been fabricated, and characterized. Both pressure sensors and modulators have been built using stainless steel as a substrate and a combination of lamination and traditional micromachining processes as fabrication technologies.

Introduction

Micromachined devices have been primarily realized using silicon substrates [1]. In many applications, the use of traditional silicon-substrate micromachined devices may be limited, for example by the lack of ability of the surrounding silicon substrate to absorb large mechanical shocks. In this work, we have investigated the use of more robust substrates as suitable starting points for both bulk and surface micromachined structures, as well as investigated the possibility of the substrate forming essential structural components of the device package. Alternative fabrication techniques, such as techniques more commonly used in either conventional machining as well as electronic packaging fabrication (e.g., lamination), are combined with more traditional integrated-circuit-based microelectronics processing techniques to create micromachined devices on these robust substrates.

One of the advantages of the use of robust substrates is the possibility of co-fabrication of the micromachined devices and their packages using, e.g., the robust substrate itself as an integral part of the sensor package. Another advantage is that due to substrate robustness, these co-packaged devices may be able to be used in mechanically harsh environments, such as aerodynamic applications. Finally, it is envisioned that the larger-scale devices

(especially actuators) producible by this fabrication technology will have increased control authority over their silicon counterparts.

The use of synthetic jets [2] as fluidic actuators enables the possibility of altering the apparent aerodynamic shape of an airfoil by creating a closed recirculation region without extending any mechanical parts into the crossflow of the airfoil. This approach is very suitable for a MEMS-based flow control scheme, since (1) such devices have already been demonstrated as being compatible with micromachining technology [3]; and (2) the relatively 'delicate' MEMS devices do not need to be exposed to the flow; in fact, the devices can be recessed under an orifice plate, safely out of reach of the flow. A microjet, pressure sensor, and provision for integrated circuitry can also be combined together to form a module suitable for repetition into an array. Such a module contains a modulator to switch the synthetic jets on and off at each orifice hole, a pressure sensor to sense the local pressure, and some local electronics to perform readout, signal linearization, and/or local control. In this first year of the project, we have focused on the following goals: (1) development of the fabrication technology for realization of robust micromachined devices; (2) development of pressure sensor arrays based on these technologies; (3) development of microjet modulators based on these technologies; and (4) feasibility demonstration of the integration of electronics with devices based on these technologies.

Pressure sensor development

A robust capacitive pressure sensor array has been fabricated using stainless steel as a substrate, Kapton film as a pressure-sensitive flexible plate, and electroplated nickel as a back electrode. By sensing the capacitance change of the capacitor formed between the flexible diaphragm and the rigid backplate (Figure 1), and by knowing the mechanical properties of the diaphragm, the pressure can be determined. An important attribute of this design is that only the steel substrate and the pressure sensor inlet is exposed to the flow; i.e., the sensor is self-packaged.

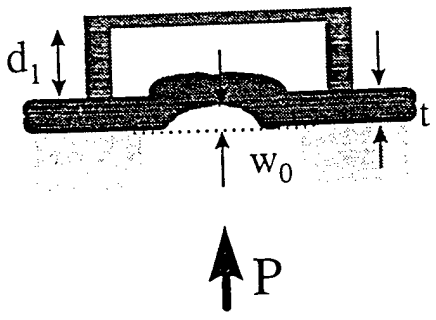

Figure 1. A schematic diagram of the side-view of the capacitive pressure sensor.

The sensor device concept is based on the pressure-induced deflection of a metallized flexible plate and the subsequent measurement of the capacitance between this deflecting plate and a fixed surface micromachined backplate positioned over the plate. Figure 1 shows a schematic diagram of the side-view of the device, where d_1 is an initial gap distance between the fixed back electrode and the flexible plate electrode, w_o is the deflection at the center of the plate, t is the thickness of the plate, and P is the uniform applied pressure. For analytical modeling [4], several assumptions have been made: (1) neglect stretching of the plate; (2) neglect the thickness of the metallic electrode on the plate; (3) neglect residual stress in the plate; and (4) neglect electric field fringing effects. Under these conditions, the capacitance-pressure relationship of the sensor can be shown to be:

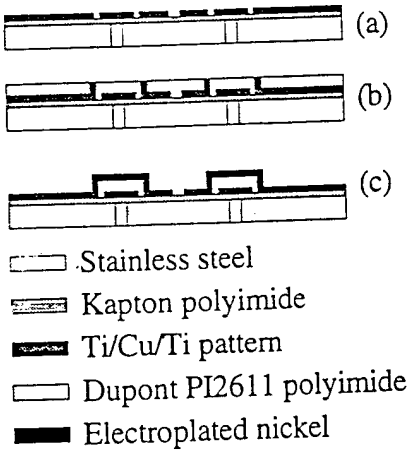

Figure 2. Pressure sensor fabrication sequence.

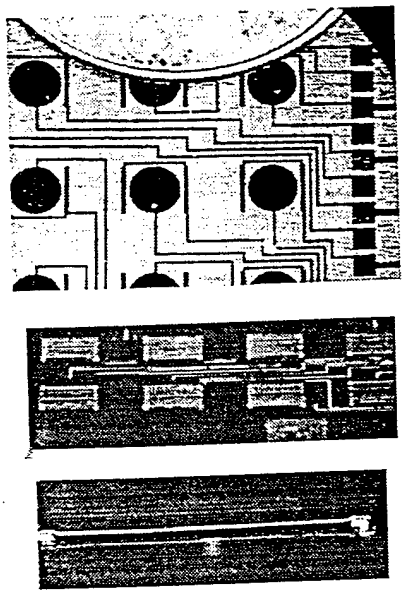

Figure 3. Photomicrographs of fabricated pressure sensors. (a)top, diaphragm prior to backplate; (b) middle, backplate view; (c)bottom, backplate gap close view

$$C_{sensor} = C_0\left(1 + K_1 P + K_2 P^2 + \cdots\right), \qquad (1)$$

where K_n are constants given by:

$$K_n = \frac{1}{(2n+1)}\left[\frac{a^4}{64Dd_1}\right]^n, \qquad (2)$$

for n≥1, C_0 is the undeflected capacitance, a is the radius of the diaphragm, and D is the flexural rigidity of the diaphragm.

The fabrication sequence of the robust pressure sensor array is shown in Figure 2. The process starts on square 5.7 cm (2 inch) on a side, 0.5 mm (20 mil.) thick stainless steel substrates. An array of 8x8 pressure inlet holes with a diameter of 2 mm, with 5 mm center-to-center distances, are milled through the substrate. Kapton film (Dupont, Kapton HN200, 50μm [2 mil.] thick) is laminated onto the milled substrate using a hot press. The pressure sensitive flexible plates will be the Kapton film in the regions suspended over the milled pressure inlet holes. A triple metallic layer of Ti/Cu/Ti with a thickness of 100/2,000 /500 Å is deposited on the surface of the Kapton film and then patterned to create bottom electrodes, electroplating seed layers, and bonding pads (Figures 2a and 3a). Multiple layers of PI2611 polyimide (Dupont) are spun onto the patterned layer, and hard-cured in a N_2 ambient at 300 ^{O}C yielding a final thickness of polyimide of approximately 44~48 μm. The polyimide layer is etched to create electroplating molds and nickel supports are then electroplated through the molds (Figure2b). A Ti/Cu/Ti metallic triple layer is deposited to act as a seed layer for the deposition of the backplate. Thick photoresist (Shipley PR 5740) is spun on the seed layer (approximately 15 μm thick) and patterned to act as electroplating molds. Nickel is electroplated through the molds to create the backplates. The thick photoresist and the remaining seed layer is removed. Finally, the polyimide sacrificial layers are isotropically etched to create air gaps between the fixed backplates and the pressure sensitive Kapton polyimide flexible plates (Figures 2c and 3b, c). The isotropic dry etch is carried out in a barrel plasma etcher using CF_4/O_2 plasma.

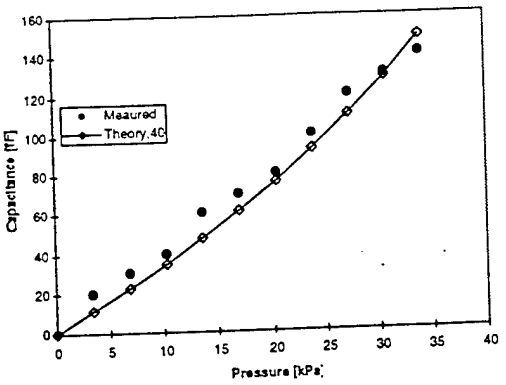

Figure 4. Theoretical and measured values of net capacitance change.

The capacitance of individual pressure sensors has been measured using a Keithley 3322 LCZ meter. Measured capacitances for undeflected pressure sensors were in the range from 11.35 pF to 13.97 pF depending on the length of interconnections between bonding pads and sensors. Over an applied pressure range from 0 to 34 kPa, the net capacitance change was approximately 0.14 pF. Theoretical prediction of the sensor behavior is determined by taking the first three terms of equation (1) (i.e., up to n=2). The theoretical data shown in Figure 4 is based on an initial gap (d_1) of 40 μm. There is approximately a 10~20 % difference between the measured physical gap and the 40 μm gap value used to provide a best fit between theory and experiment. This difference could be explained by the fringing effects of the sensor capacitance. The measured values of relative capacitance change are in the range from 1% to 1.34 %.

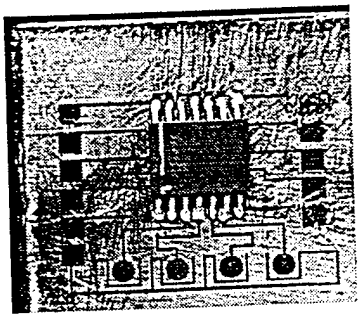

Figure 5. A photomicrograph of the surface-mount chip integrated on laminated Kapton film.

The values of capacitance and/or corresponding frequency changed produced by the sensors are easily measurable in their current form; however, in order to achieve higher sensitivity, elimination of parasitic capacitance is essential. Parasitic capacitance can be eliminated by using integrated on-chip circuitry which has a reference electrode, which has same structure as that of a pressure sensor with a pressure insensitive (immovable) circular plate. With a goal of achieving such an integrated on-chip circuitry, a demonstration example has been fabricated (Figure 5). In this figure, surface-mounting 14-pin chip has been integrated on patterned metallic lines on Kapton polyimide film which is laminated on stainless steel substrate. This physical demonstration shows the feasibility of the concept of the control and drive circuitry directly integrated on microfabricated fluidic systems.

Microjet modulator development

A robust microjet modulator array has been fabricated using stainless steel as a substrate, Kapton film as an insulator, and thin stainless steel foil (50 μm thick) as the modulator material. Microjet drivers have been assembled with these robust modulators and the velocity profiles of the MEMS-modulated synthetic jets for multiple numbers of modulators in an array has been measured using particle image velocimetry (PIV). The modulators operate by electrostatically opening and closing a plate which bears an array of holes and which covers the orifice plate. When the plate is in contact with the substrate, the substrate orifice hole is blocked and the synthetic jet cannot issue from the

orifice. When the plate is not in contact with the substrate, the synthetic jet can flow through the holes in the orifice plate and through the orifice hole in the substrate, thereby allowing a synthetic jet to issue from the orifice hole.

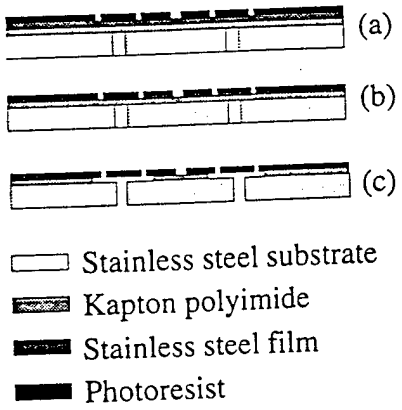

Figure 6. Modulator fabrication sequence.

The fabrication sequence of the robust modulator array is shown in Figure 6. The process starts on square 5.7 cm (2 inch) on a side, 0.5 mm (20 mil.) thick stainless steel substrates. An array of 5x5 orifice holes with a diameter of 2 mm, with 10 mm center-to-center distances, are milled through the substrate. Kapton film (Dupont, Kapton HN200, 50μm [2 mil.] thick) is laminated onto the milled stainless steel using a hot press. Stainless steel foil (50 μm [2 mil.] thick: AISI-T302) is laminated again on top of the Kapton polyimide film using a hot press. Photoresist SC1813 (Shipley) is spun onto the laminated stainless steel foil. Photoresists are photo-defined and the stainless steel metal foil is wet etched. The modulation actuators will thus be formed by the stainless steel foil in the regions suspended over the milled orifice holes. The Kapton film has been isotropically dry etched using a barrel plasma etcher. Finally, a 5.6 μm thick parylene film is conformally deposited for electrical insulation.

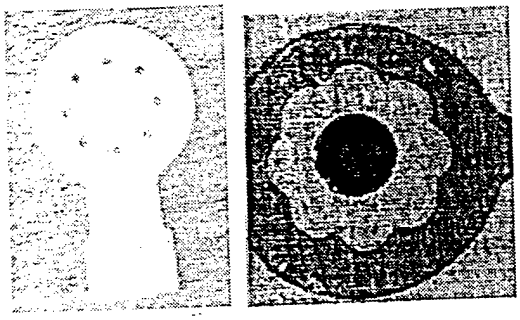

Figure 7. (Left) Top view of the stainless steel modulator after the wet etching (Right) Top view of the etched profile of Kapton polyimide film after isotropic dry etch.

After the fabrication of an array of robust modulator, the modulator array has been assembled with microjet drivers (Figure 8). Both electromagnetic and piezoelectric drivers have been assembled and tested. The assembled robust modulator/jet driver has been tested using particle image velocimetry (PIV). Figure 9 shows raster plots of the velocity magnitude for three modulators with different diameter vent holes (the vent holes of the modulator at 10 mm [x-axis] is the largest and the one at 30 mm is the smallest) with all modulators open. This PIV test result shows that the robust modulator/jet driver can create jets with centerline speeds at $y/d \approx 10$ (where d is the diameter of the orifice hole) of as much as 6 m/s.

Conclusions

Robust materials have been studied as suitable substrates for micromachined devices. Lamination combined with traditional micromachining processes, has been investigated as a suitable fabrication process for the robust substrates.

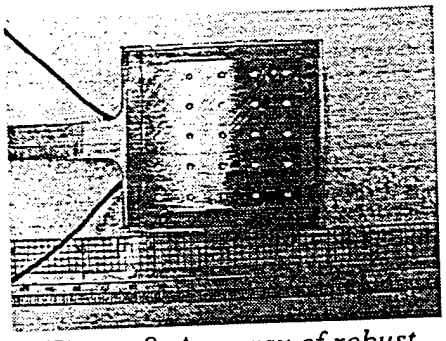

Figure 8. An array of robust modulators assembled with a central microjet driver, showing the array of orifice holes. This view is what the external crossflow 'sees'.

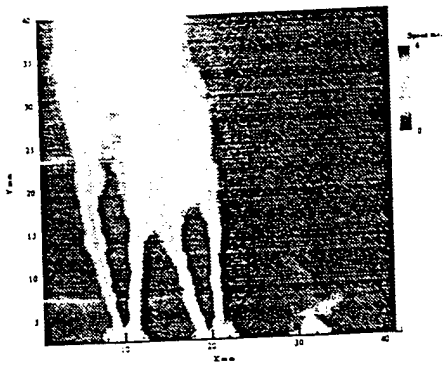

Figure 9. Velocity profile (PIV data) for the robust modulator array (three modulators with different diameters of vent holes shown).

A capacitive pressure sensor array using a robust stainless steel shim stock, Kapton plate, and lamination processing has been designed, fabricated, and characterized. Detection circuitry has been designed and integrated with pressure sensors in a hybrid fashion to provide frequency-modulated output. It has been shown that surface-mount chips can be directly integrated on robust micromachined devices to make higher sensitivity devices.

A robust modulator array using a robust stainless steel shim stock, Kapton film as an insulator, stainless steel metal foil as a modulator body has been designed, fabricated, and characterized. The PIV test for parts of robust modulator arrays show that microjets as high as 6 m/s can be created using this device.

Acknowledgement/Disclaimer

This work was sponsored in part by the Air Force Office of Scientific Research, USAF, under grant/contract number F49620-97-1-0519. The views and conclusions contained herein are those of the authors and should not be interpreted as necessarily representing the official policies or endorsements, either expressed or implied, of the Air Force Office of Scientific Research or the U.S. Government.

References

[1] H. Baltes, "CMOS micro electro mechanical systems," *Sensors and Materials*, vol. 9, no. 6, pp.331-346, 1997.

[2] R. D. James, J. W. Jacob, and A. Glezer, "A round turbulent jet produced by an oscillating diaphragm," *Journal of Physics of Fluids*, vol. 8, no. 9, pp. 2482-2495, 1996.

[3] D. J. Coe, M.G. Allen, M.A. Trautman, and A. Glezer, "Micromachined jets for manipulation of macro flows" in *Proceedings 1994 Solid-State Sensors and Actuators Workshop*, Hilton Head, SC, 1994, pp.243-247.

[4] S. Timoshenko, "*Theory of Plates and Shells*," McGraw-Hill Book Company, New York, 1940.

Presented at 1999 AFOSR Contractor Review Meeting

DEMONSTRATION OF ROBUST MICROMACHINED JET TECHNOLOGY AND ITS APPLICATION TO REALISTIC FLOW CONTROL PROBLEMS

AFOSR GRANT F49620-97-1-0519

Mark G. Allen and Ari Glezer
School of Electrical and Computer Engineering &
School of Mechanical Engineering,
Georgia Institute of Technology, Atlanta, GA

Abstract

In this work, we are investigating the use of microfabrication technology to create a micromachined fluidic control system (consisting of micromachined actuators, sensors, and control/drive circuitry) with a goal of application in practical fluids problems, such as UAV-scale aerodynamic control. Our approaches include: (1) the development of suitable micromachined synthetic jets (*microjets*) as actuators, which obviate the need to physically extend micromachined structures into an external flow; and (2) a non-silicon alternative micromachining fabrication technology based on metallic substrates and lamination (in addition to traditional MEMS technologies) which will allow the realization of larger scale, more robust structures and larger array active areas for fluidic systems. As an initial study, an array of MEMS pressure sensors and an array of MEMS modulators for orifice-based control of microjets have been fabricated, and characterized. Both pressure sensors and modulators have been built using stainless steel as a substrate and a combination of lamination and traditional micromachining processes as fabrication technologies.

Introduction

Micromachined devices have been primarily realized using silicon substrates [1]. In many applications, the use of traditional silicon-substrate micromachined devices may be limited, for example by the lack of ability of the surrounding silicon substrate to absorb large mechanical shocks. In this work, we have investigated the use of more robust substrates as suitable starting points for both bulk and surface micromachined structures, as well as investigated the possibility of the substrate forming essential structural components of the device package. Alternative fabrication techniques, such as techniques more commonly used in either conventional machining as well as electronic packaging fabrication (e.g., lamination), are combined with more traditional integrated-circuit-based microelectronics processing techniques to create micromachined devices on these robust substrates.

One of the advantages of the use of robust substrates is the possibility of co-fabrication of the micromachined devices and their packages using, e.g., the robust substrate itself as an integral part of the sensor package. Another advantage is that due to substrate robustness, these co-packaged devices may be able to be used in mechanically harsh environments, such as aerodynamic applications. Finally, it is envisioned that the larger-scale devices (especially actuators) producible by this fabrication technology will have increased control authority over their silicon counterparts.

The use of synthetic jets [2] as fluidic actuators enables the possibility of altering the apparent aerodynamic shape of an airfoil by creating a closed recirculation region without extending any mechanical parts into the crossflow of the airfoil. This approach is very suitable for a MEMS-based flow control scheme, since (1) such devices have already been demonstrated as being compatible with micromachining technology [3]; and (2) the relatively 'delicate' MEMS devices do not need to be exposed to the flow; in fact, the devices can be recessed under an orifice plate, safely out of reach of the flow. A microjet, pressure sensor, and provision for integrated circuitry can also be combined together to form a module suitable for repetition into an array. Such a module contains a modulator to switch the synthetic jets on and off at each orifice hole, a pressure sensor to sense the local pressure, and some local electronics to perform readout, signal linearization, and/or local control.

In the previous report we concentrated on sensor development, and have recently published a paper on the pressure sensor technology (Ref. 4). This report covers progress from July 1998 to July 1999, and is divided into three sections: progress in robust micromachining technology, specifically for the robust

microjet modulator and the robust pressure sensor; and progress in synthetic jet technology, specifically, vortex generation for aerodynamic control using synthetic jets. By incorporating conventional machining technology with lamination and surface micromachining, robust actuators were achieved. The Kapton diaphragm used for the first generation of pressure sensors was replaced by a stainless steel diaphragm.

1. Progress in robust microjet modulator technology

The actuator concept being pursued is shown in Fig. 1. Sheets of material are laminated onto a stainless steel substrate, lithographically patterned, and surface micromachined to form standoffs and flow channels. The flow channels permit airflow through an orifice conventionally machined in the substrate when the actuators are in the 'off' position. When the actuators are energized, the flexible sheet is deflected toward the surface, constricting the airflow and ultimately blocking the orifice. Currently, the actuators are driven electrostatically, by application of a voltage between the flexible sheet and the substrate. Synthetic jets are formed by addition of a piezoelectric driver attached to the actuator side of the substrate orifice. Centerline velocities on the order of 3 m/s have been measured through the three types of actuators as will be described later.

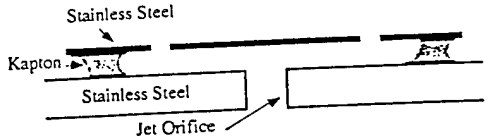

Figure 1. Schematic cross-section of robust microjet modulator

Actuator Fabrication

The devices (Fig. 2) are fabricated using lamination technology, and are made from stainless steel (SS) substrates and diaphragms, and polyimide standoffs. The process begins with a 0.05 inch milled stainless steel substrate, Kapton polyimide film, and 12.5 μm SS 302 foil. The milled substrate is 2" x 2" with 25 milled holes 2 mm in diameter. The Kapton is Type 200 HN from Dupont, and the SS302 thin film is a prefabricated, over-the-counter shim stock. To fabricate the actuators, the Kapton is first laminated to the milled substrate, and the SS foil is laminated to the Kapton. This is done in two steps for improved adhesion between each layer. Next, photolithography is used to mask the stainless steel sheet for wet etching. The stainless steel is formed into three different types of actuator geometries using a wet etch. Finally, the Kapton is removed using an isotropic dry etch, in which the stainless steel film serves as the mask for surface micromachining of the underlying Kapton. By sizing the geometries of the modulator appropriately, patterning of the Kapton sacrificial layer to form anchor points is avoided. A photograph of a two inch substrate bearing stainless steel modulators is shown below. Some of the modulators have been removed to show the underlying orifice holes.

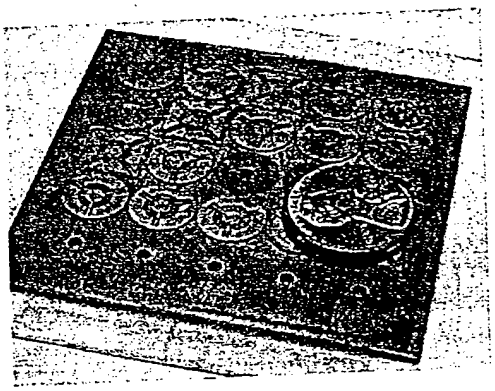

Figure 2. Photograph of modulator

Actuator geometry and performance

The actuating diaphragms consist of a central 'pad' region, which acts to cover up the orifice holes, and support beams of a variety of geometries shown in Fig. 3. For all actuators, the pad is 3.6 mm in diameter, and is designed to deflect 50 μm (the standoff height) to block the 2 mm orifice hole on the milled substrate. Each actuator has four beams extending normally outward at angles of 0°, 90°, 180°, and 270°. Also, all beam widths on the actuators are 200 μm. Geometric representations of the designed actuators are shown in the figure below. The first actuator tested has beams 1.5 mm long extending outward from the center actuator pad. This actuator had an actuation voltage of 157 V and a first resonant frequency of 384 Hz. The second type of actuator has an "S-shaped" arm with a total length of 1.4 mm. It had an actuation voltage of 550 V and a first resonant frequency of 1.145 kHz. The third actuator had an "S-shaped" beam with a total length of 2.75 mm. It had an actuation voltage of 320 V and a first resonant frequency of 409 Hz.

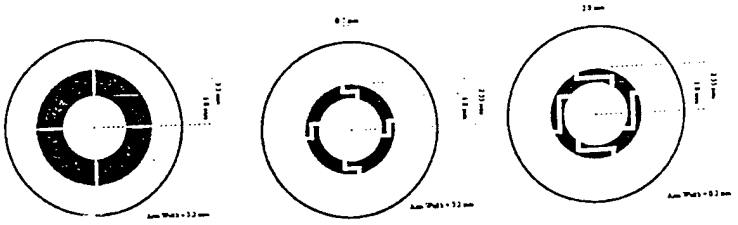

Figure 3. Three different shapes of modulators

Verification of operation using PIV

Particle image velocimetry (PIV) tests were performed on the modulator actuators, both to demonstrate that synthetic jet flow could pass through the modulators, as well as to demonstrate modulator-based control of the synthetic jet flow. Both a single modulator test (in which one isolated modulator was turned 'on'), and a dual modulator test (in which one of two adjacent modulators was turned 'on') were performed.

For the single valve PIV test, the third modulator type (2.75 mm total length) described above was used, and the piezo-driver was driven at 900 kHz. Centerline velocity from the orifice was measured at 3 m/s before electrostatic actuation (i.e., before the pad was drawn down to cover the orifice hole; figure left) and ~0 m/s once actuated (figure right). This experiment demonstrates that the modulator can physically stop a flow by controlled actuation.

The dual valve PIV tested the actuation of one valve when two valves were open, and this test used the second modulator described above (1.4mm total beam length). In this test, the centerline velocities were once again measured to be ~3 m/s when open (figure left). When one valve was actuated, the centerline velocity through the second hole remained constant and no additional vectoring was experienced (figure right).

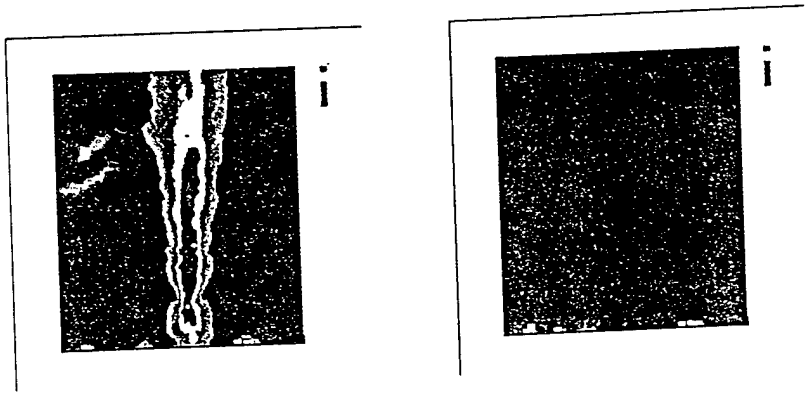

Figure 4. Single and dual modulator test using PIV.

2. Progress in robust pressure sensor technology

In the last report, a robust capacitive pressure sensor array was demonstrated. It used stainless steel as a substrate, Kapton film as a pressure-sensitive flexible plate, and electroplated nickel as a back electrode. By sensing the capacitance change of the capacitor formed between the flexible diaphragm and the rigid backplate (Figure 5), and by knowing the mechanical properties of the diaphragm, the pressure can be determined. An important attribute of this design is that only the steel substrate and the pressure sensor inlet is exposed to the flow; i.e., the sensor is self-packaged [4]. A critical point in this design was that Kapton was exposed to the flow. We report an improved fabrication technology, which uses a stainless steel diaphragm, thus ensuring that only stainless steel is exposed to the flow.

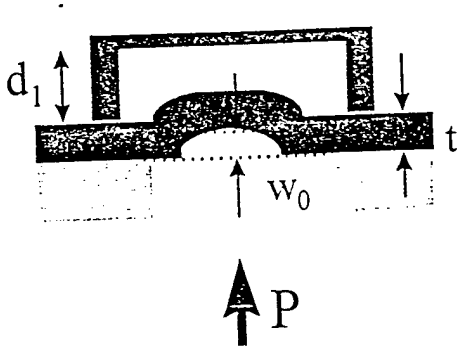

Figure 5. A schematic diagram of the side-view of the capacitive pressure sensor.

Figure 5 shows a schematic diagram of the side-view of the device, where d_1 is an initial gap distance between the fixed back electrode and the flexible plate electrode, w_o is the deflection at the center of the plate, t is the thickness of the plate, and P is the applied uniform pressure. An analytical model is shown in [4].

Fabrication of robust pressure sensor

The fabrication sequence of the robust pressure sensor starts on a square stainless steel substrate. Its side length and thickness are 5.7 cm (2 inch) and 0.5 mm (20 mil.), respectively. An array of 8x8 pressure inlet holes with a diameter of 2 mm, with 5 mm center-to-center distances, are milled through the substrate. A Kapton film (Dupont, Kapton HN200, 50μm [2 mil.] thick) and a stainless steel film are laminated onto the milled substrate using a hot press. The pressure sensitive flexible plates will be the stainless steel film in the regions suspended over the milled pressure inlet holes. Next a polyimide (PI) isolation layer is deposited with a thickness of 3μm. To create bottom electrodes, electroplating seed layers, and bonding pads (Figure 6), a triple metallic layer of Ti/Cu/Ti is deposited with a thickness of 250/6000/250 Å and patterned. Two layers of AZ4620 photoresist are spun onto the patterned layer, yielding a final thickness of photoresist of approximately 40~45 μm. The photoresist is patterned to create electroplating molds and nickel supports are electroplated through the molds. To fabricate the backplate, a Ti/Cu/Ti metallic triple layer is deposited to act as a seed layer. Thick photoresist (AZ 4620) is spun on the seed layer (approximately 20μm thick) and patterned to act as electroplating molds. Nickel is electroplated through the molds to create the backplates. Finally, the photoresist sacrificial layers and the seed layer in between them are etched using Acetone to create an air gap between the fixed backplate and the pressure sensitive stainless steel diaphragm (Figure 5). Finally the Kapton underneath the stainless steel diaphragm is removed by dry etch using RIE.

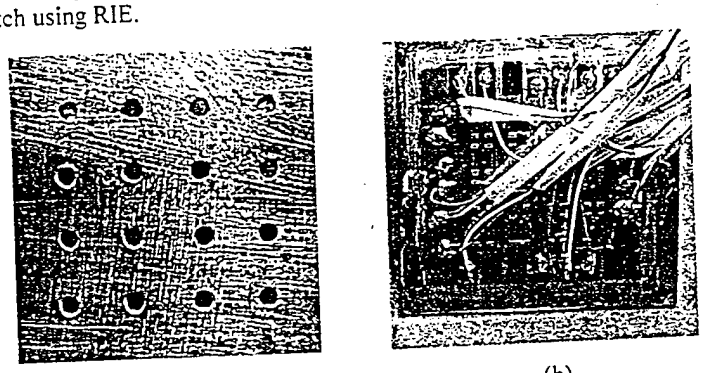

(a) (b)

Figure 6. Photomicrographs of fabricated pressure sensors. (a) side exposed to flow. (b) sensor view.

Measurement

The capacitance of individual pressure sensors has been measured using a Keithley 3322 LCZ meter. Measured capacitances for undeflected pressure sensors were in the range 59pF to 95pF depending on the length of interconnections between bonding pads and sensors. The electronics chosen to read out the pressure sensors is an astable multivibrator, the frequency of which depends on the capacitance of the sensor. We have achieved this integration by using surface mount components; both operational amplifiers and surface-mount external resistors for the multivibrator circuit.

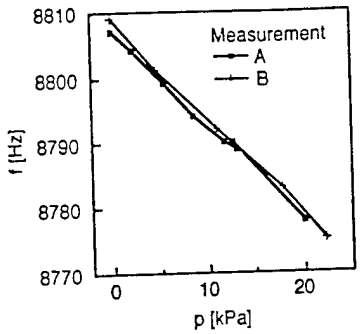

Figure 7: Theoretical and measured values of net capacitance change.

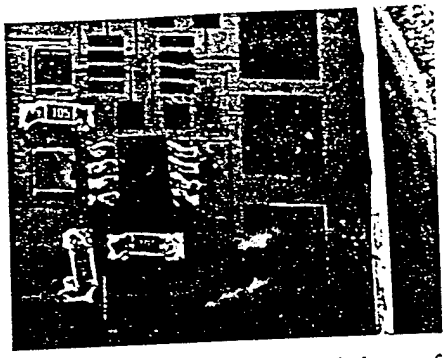

Figure 8. A photomicrograph of the surface-mount chip integrated on laminated Kapton film.

Specific improvements since the last report are:

1. The wiring paths have been reconfigured to minimize the parasitic capacitances.

2. Surface-mount passive components have been integrated in the system (in the previous reporting period, the passive components were external). The sensitivity of the pressure sensor is typically -1.48 Hz kPa^{-1}.

The values of capacitance and/or corresponding frequency change produced by the sensors are easily measurable in their current form. However, in order to achieve higher sensitivity, reduction of the parasitic capacitance is desirable. Furthermore, a multiplexing scheme to address larger numbers of sensors using a control bus has to be developed. We are currently investigating feasibility of flip-chip bonding as well as wire-bonding of the silicon circuitry.

3. Progress in synthetic-jet-based vortex generation for aerodynamic control

The operational range of fixed vortex generators and of vortex generator jets can be substantially extended by using synthetic jet actuators of the type achievable using robust substrate micromachining. An important attribute of these jets is that when they are operated in close proximity in phased arrays (which can be achieved using MEMS technology), they can be cooperatively vectored simply by adjusting the relative phase of their individual control signals. A non-zero phase angle between adjacent jets results in a combined jet that vectors toward the jet that is leading in phase, thus leading to the formation of either clockwise or counterclockwise vorticity.

In the present work, each vortex generator module is comprised of a pair of adjacent jets emanating out of rectangular (300 μm wide) orifices that are parallel along their long (streamwise) dimension and are 1.25 mm apart. The interaction of three jet pairs in the absence of a cross flow is shown in PIV (particle image velocimetry) images in Fig. 9. These images are color raster plots of the velocity magnitude (ranging from 0-3.5 m/s) in the spanwise cross flow (y-z) plane. In the figure below left, all three jet pairs are driven in phase and are nominally normal to the surface. In the figure below right, the right hand side jet in each pair

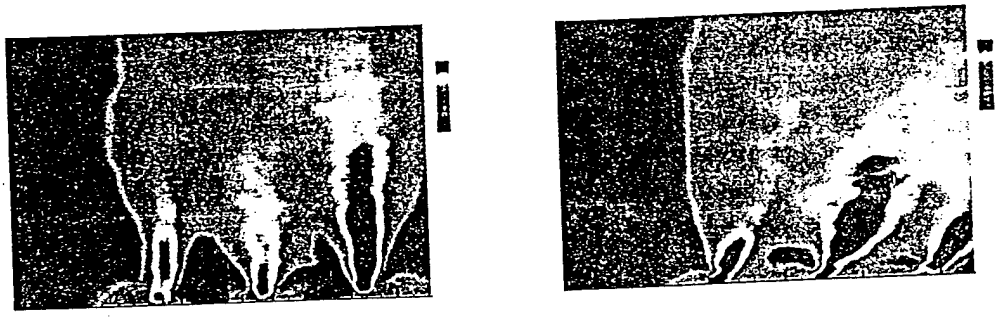

Figure 9: Velocity magnitude plot of vectored microjets

is leading in phase (by 80°) and the resultant jets are all vectored to the right. Other spanwise jet interactions are easily software-programmed by altering the relative phase angle of each pair.

An investigation of the evolution of vectored synthetic jets in a cross-flow is conducted in a small-scale wind tunnel where the jet array module is integrated into the test section floor. In the spanwise (x-y) view, the vertical and spanwise velocity components are captured and thus it is possible to compute directly the sense and strength of the streamwise vorticity. Data is taken at a number of streamwise stations. Figure 10 show superposed images of the velocity vectors in the y-z plane and color raster plots of the streamwise vorticity for a single jet pair taken at x/L = 3 (L is the streamise length of the jet orifice). In the center figure, the phase angle is 0 and the data shows almost no traces of streamwise vorticity. In the right figure the right hand side jet is leading in phase by 130° and the vectoring is to the right leading to the formation of a strong counter-clockwise vortex. When the phase angle is reversed (left) the sense of the streamwise vortex is reversed (i.e., clockwise). Note the appearance of vorticity of the opposire sense in each image next to the tunnel wall owing to the induced boundary layer.

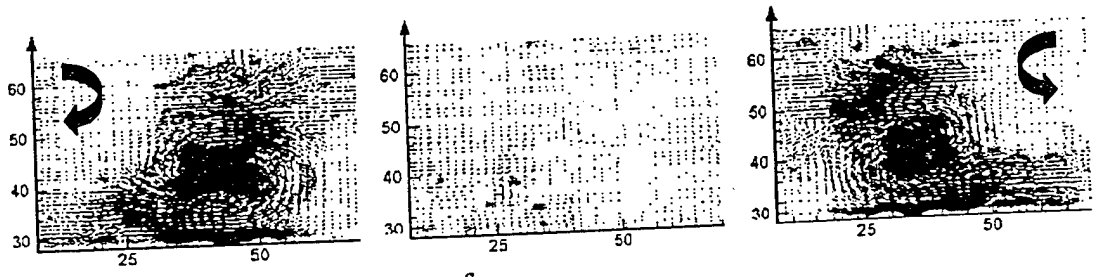

Figure 10: Vectored synthetic jets in a cross-flow

Conclusions

Robust materials have been studied as suitable substrates for micromachined devices. Lamination combined with traditional micromachining processes, has been investigated as a suitable fabrication process for the robust substrates.

A capacitive pressure sensor array using a robust stainless steel shim stock, stainless steel diaphragm, and lamination processing has been designed, fabricated, and characterized. Read-out circuitry has been designed and integrated with the pressure sensors, providing a frequency-modulated output. Surface-mount chips were directly integrated on robust micromachined devices to make high sensitivity devices.

A robust modulator array using a robust stainless steel shim stock, Kapton film as an insulator, stainless steel metal foil as a modulator body has been designed, fabricated, and characterized. The PIV tests for parts of robust modulator arrays show that microjets as high as 6 m/s can be modulated using this device.

Acknowledgement/Disclaimer

This work was sponsored in part by the Air Force Office of Scientific Research, USAF, under grant/contract number F49620-97-1-0519. The views and conclusions contained herein are those of the authors and should not be interpreted as necessarily representing the official policies or endorsements, either expressed or implied, of the Air Force Office of Scientific Research or the U.S. Government.

References

[1] H. Baltes, "CMOS micro electro mechanical systems," *Sensors and Materials*, vol. 9, pp.331-346, 1997.

[2] R. D. James, J. W. Jacob, and A. Glezer, "A round turbulent jet produced by an oscillating diaphragm," *Journal of Physics of Fluids*, vol. 8, no. 9, pp. 2482-2495, 1996.

[3] D. J. Coe, M.G. Allen, M.A. Trautman, and A. Glezer, "Micromachined jets for manipulation of macro flows" in *Proceedings 1994 Solid-State Sensors and Actuators Workshop*, 1994, pp.243-247.

[4] Chang, S.P., Lee, J.B., and Allen, M.G., "A Robust 8x8 Capacitive Pressure Sensor Array," proceedings of the 1998 Annual Meeting of the ASME, 1998.

DEMONSTRATION OF ROBUST MICROMACHINED JET TECHNOLOGY AND ITS APPLICATION TO REALISTIC FLOW CONTROL PROBLEMS

Mark G. Allen and Ari Glezer
School of Electrical and Computer Engineering & School of Mechanical Engineering,
Georgia Institute of Technology, Atlanta, GA

Abstract

In this work, we are investigating the use of microfabrication technology to create a micromachined fluidic control system (consisting of micromachined actuators, sensors, and control/drive circuitry) with a goal of application in practical fluids problems, such as UAV-scale aerodynamic control. Our approaches include: (1) the development of suitable micromachined synthetic jets (*microjets*) as actuators, which obviate the need to physically extend micromachined structures into an external flow; and (2) a non-silicon alternative micromachining fabrication technology based on metallic substrates and lamination (in addition to traditional MEMS technologies) which will allow the realization of larger scale, more robust structures and larger array active areas for fluidic systems. In the previous report, we demonstrated independently fabricated sensors and actuators. These devices were fabricated using stainless steel as a substrate and a combination of lamination and traditional micromachining processes as fabrication technologies. This report covers the initial fabrication process of pressure sensors and microjet modulators co-integrated on the same substrate, the successful design of a switched capacitor amplifier as an interface to the pressure sensor, and advances in vortex generation.

1. Progress in Robust Micromachining Technology

Figure 1 shows a robust modulator and pressure sensor co-integrated on the same stainless steel substrate. The sensor contains a stainless steel membrane extended over the pressure inlet hole. When pressure is applied, the membrane deflects toward the fixed back plate. This increases the capacitance between membrane and back plate. The actuator contains a disc, supported by three or four beams. The channel between the disc

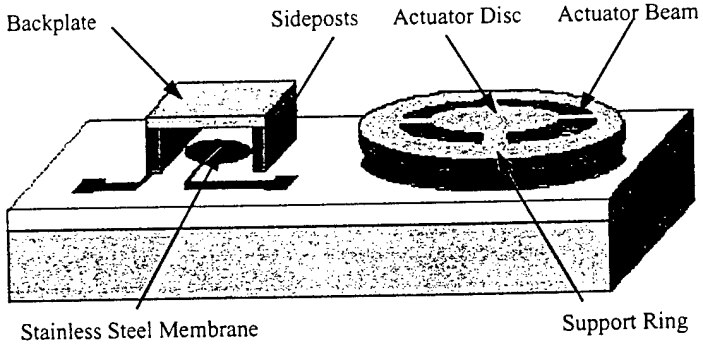

Figure 1: System of robust pressure sensor (L) and microjet modulator (R).

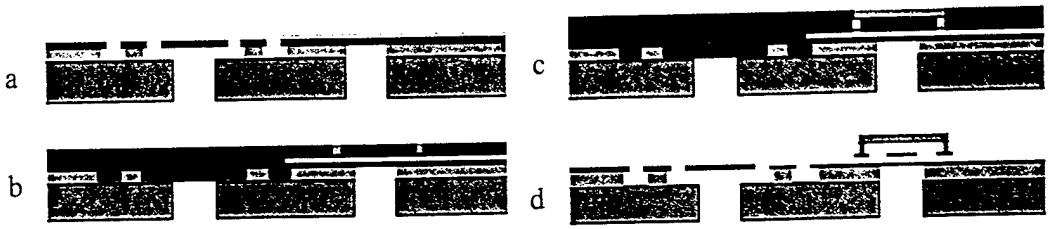

Figure 2: Fabrication sequence for sensors and actuators.

and an orifice conventionally machined in the substrate permits airflow when the actuator is in the 'off' position. When the actuator is energized, the disc is deflected toward the substrate, constricting the airflow and ultimately blocking the orifice. Currently, the actuators are driven electrostatically, by application of a voltage between the flexible sheet and the substrate. Synthetic jets are formed by addition of a piezoelectric driver attached to the actuator side of the substrate orifice.

The co-fabrication sequence of robust pressure sensors and robust modulators starts on a square stainless steel substrate with a side length and thickness of 60mm and 0.9 mm, respectively. Pressure inlet and jet holes with diameters of 2mm are milled through the stainless steel substrate. Figure 2 shows the fabrication sequence in greater detail.

A 50μm thick Kapton HN200 polyimide film and 12.5μm stainless steel film are laminated on the milled stainless steel substrate using a hot press. To form the actuator disc, the support ring, and the actuator beam, polyimide 2611 is spin coated on the stainless steel film, cured and patterned. Then the stainless steel film is etched. Next, the Kapton film under the stainless steel film is dry-etched through the backside holes of the sensors and actuators. The Kapton under the suspensions of the actuator plates is etched from the front side. (Fig. 2a).

Then the bonding pads, interconnection lines and bottom electrodes, and the seed-layers for the electroplating steps are formed. Ti/Cu/Ti (300/6000/300A°) is deposited and patterned. Positive photoresist AZ 4620 forms the molds of the side posts of the sensor. Finally, NiFe is electroplated through the mold (Fig. 2b).

To fabricate the back plate of the sensor, a seed-layer is deposited and patterned. AZ 4620 positive photoresist defines a mold. Then NiFe is electroplated, (Fig. 2c). Finally the two photoresist layers, and the second seed layer are removed, (Fig. 2d). The final system of sensors and actuators is shown in Figure 3.

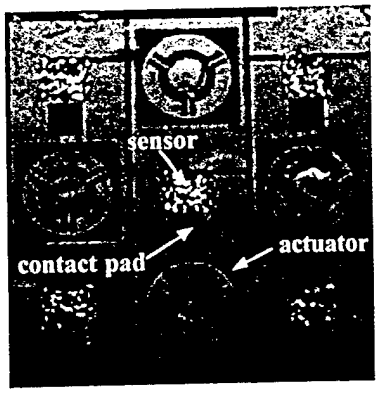

Figure 3: Photograph of fabricated sensor and actuator array.

Characterization

The capacitance of individual pressure sensors has been measured using a Keithley 3322 LCZ meter. Measured capacitances for undeflected pressure sensors were in the range of

73.4 pF to 93.5 pF. A large fraction of these values originates from parasitic capacities of the connection lines and bonding pads on the substrate. The capacitance change as a function of applied pressure is shown in the Figure 4.

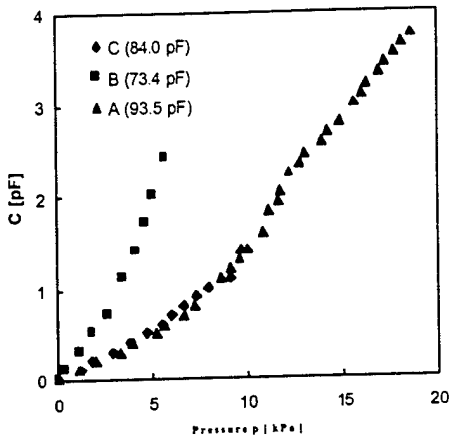

Figure 4: Capacitance of sensors as a function of applied pressure.

The modulators co-fabricated with the pressure sensors do not yet operate satisfactorily due to some fabrication issues currently under investigation. Therefore, the discussion below centers on the characterization of actuators on independently fabricated modulators with similar cross-section.

In order to reduce actuation voltages and achieve significant process yields, several parameters have been varied: beam length, gap size, actuator disc diameter d_a, and orifice diameter d_o. A new shape of the support ring, with preliminary results shown in the last report, allowed retaining the beam length while maximizing the support area. This increased the yield to 90%.To increase the electrostatic force, the effective area of the capacitor, i.e. the overlap between substrate and diaphragm can be increased. The effective capacitor area is $A_{eff} = \pi(d_a^2 - d_o^2)/4$. To increase A_{eff} the size of the orifice was reduced. The 1mm orifice devices repeatedly exhibited pull down voltages under 200 V. However, the centerline flow velocity was reduced to approximately 1 m/s. Previous testing has produced jets with centerline flow velocity of approximately 3 m/s.

We conclude that the actuation voltage of the electrostatically actuated modulators can be reduced below 200 V. Significant reduction of the voltage, however, can not be achieved without reducing the flow velocity of the air jet. To achieve better performance we are currently investigating the use of thermally actuated Cu/Ti bimorph structures to modulate microjets. For a cantilever length of 3.0 mm we get deflections of 36 µm at a heat dissipation of 235 mW.

2. Interface Circuitry for an array of Robust Pressure Sensor

The characterization of pressure sensors and the activation of modulators are both currently performed remotely. Local read-out circuitry is desirable for three reasons. First, the capacitance changes of a pressure sensor are small. Parasitic capacitances and pick-up of noise through the connection cables induce measurement errors. Second, a bandwidth of 1kHz should be achieved to resolve aerodynamic fluctuations of the pressure. In the previous report we demonstrated an oscillator built in proximity to the sensor, based on discrete components. Its resonance frequency depends on the capacitance of the pressure sensor, which is used to measure the pressure. This scheme is accurate if the integration time of the frequency counter is larger than 0.1s. The method can not resolve aerodynamic pressure fluctuations. An additional restriction of this approach is that only one sensor can be interfaced with the circuit.

We designed and characterized a custom ASIC that solves these two limitations. One of four sensors can be selected. The chip uses a standard switched capacitor (SC) architecture to measure the difference between the capacitance of the selected sensor and an on-chip reference. The transfer function from the sensor capacitance C_{sensor} to the output voltage V_{out} is the following

$$V_{out} - V_{cm} = -5(V_{sig} - V_{icm})\frac{C_{sensor} - C_{ref}}{C_{ref}} + 5(V_{ref} - V_{sig}),$$

where the reference capacitance C_{ref} can be adjusted between 10pF and 70pF in seven steps to compensate for the process dependent sensor capacitance at zero pressure. It can be further tuned by the voltage V_{ref}-V_{sig}. The voltage V_{sig}-V_{icm} determines the sensitivity.

The operational amplifier is based on a standard folded cascode architecture. At a bias current of 40 µA the op-amp dc power consumption is 1.2mW. The open loop gain is 62dB and the gain bandwidth product is 11.9MHz with a phase margin of 59° for a load capacitance of 5pF. The first and second poles are at 12kHz and 32MHz, respectively. With a SC feedback gain of 5 a gain inaccuracy of 0.4% is achieved when switch noise is neglected. For $C_{sensor} = C_{ref} = 70pF$ the bandwidth is 394kHz.

The amplifier was designed on a MOSIS ABN 1.5µm run. It was integrated with additional circuitry for clock generation, bias generation, and on-chip trimming. The total core area is 2.3 mm^2. To achieve reasonable settling, a clock speed of 50 kHz was chosen. The ASIC was characterized using a standard capacitor of 49pF instead of the sensor, a supply voltage of 4.993V, and control voltages V_{cm} and V_{sig} of 2.995V and 2.492V, respectively. The gain of V_{out} versus V_{ref} was 4.89 to be compared with 5.0 for ideal on-chip capacitor ratios and infinite op-amp gain. These chips have just been received back from the foundry. As a next step, the ASIC will be characterized together with a sensor described in Section 1.

3. On-demand Synthetic Jet Vortex Generation

Vortex generators of varying scales are widely utilized in numerous aerodynamic applications to prevent or delay flow separation by inducing the formation of streamwise vortices of a prescribed sign near the flow surface. In current realizations, vortex generators are typically made of spanwise rows of passive plates that are permanently mounted on the flow surface and thus affect the flow and contribute to the aerodynamic drag even in the absence of separation. Compton and Johnston (1992) proposed to emulate the effect of a vortex generator by using a jet that issues normal to the surface (having the advantage that it can be "removed" when not needed). Pitching or skewing of the jet relative to the oncoming flow leads to the evolution of a *single sign* streamwise vortex where the sense of the rotation is determined by the skew direction and vortex strength is determined by the skew angle. However, with a fixed nozzle, this vortex generator is limited to a fixed sign vortex.

This part of the project focuses on the development of batch-fabricated arrays of fluidic-based vortex generators that are capable of generating streamwise vortices having *prescribed sign and strength.* Each element in the array is comprised of a pair of adjacent rectangular synthetic (zero net mass flux) jets where the jet spacing (along their

long dimensions) is comparable to the width of the jet orifice. Each jet can be produced over a broad range of scales by an actuator comprised of a closed chamber having an orifice and an oscillating diaphragm that is built into one of the chamber walls. When the jets are operated in concert, the combined jet can be vectored towards one of the jets by advancing the phase of the actuation signal of that jet (Smith and Glezer[1]) resulting in a single-sign streamwise vortex where the sense of rotation and strength are controlled by the sign and magnitude of the phase difference between the driving signals. The interactions between arrays of synthetic jet pairs and a cross flow of varying speed is investigated in the cross-stream (x-y) and spanwise (y-z) planes of a small scale wind tunnel. Arrays of rectangular (0.5 mm wide, and 25 mm long) jet pairs (spaced 14 mm apart on center) are fabricated using lithographic techniques and driven using piezoelectric membranes (at 980 Hz) and integrated into the test section wall so that their axes are aligned with the streamwise (x) direction.

As the velocity ratio between the jet and the cross flow VR is decreased, the jet bends in the streamwise direction and its penetration distance into the cross flow decreases. Figures 5 is a composite of three streamwise stations for VR = 0.8 (a) and 0.48 (b). While the penetration height of the jet into the cross flow decreases, the vorticity concentrations that originate from the downstream edge of the jet orifice persist through the downstream edge of the measurement domain. These successive concentrations are advected at the speed of the free stream, and the spacing between them increases with decreasing velocity ratio (the jet frequency is invariant).

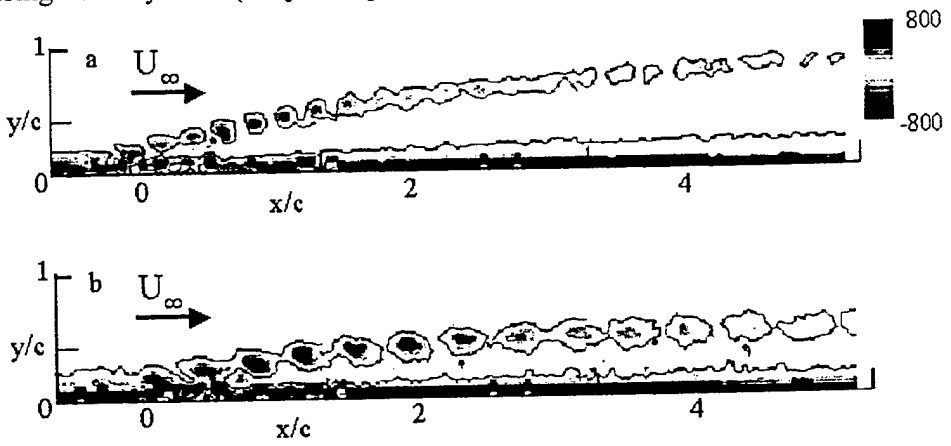

Figure 5. Jet penetration into cross flow, VR = 0.8 (a), 0.48 (b) (Negative vorticity is bounded with a single contour at lowest level.).

The evolution of the ensuing streamwise vortices in the cross-stream y-z plane (looking in the streamwise direction) is shown in Figures 6(a,b) for x/c = 3 for an array of 5 jet pairs. When the two jets in each pair are in phase, symmetric counter-rotating vortex pairs much like those of conventional jets are present (Figure 6a). These data also show pairs of secondary streamwise vortices that are induced near the wall (in the wake of the jet). Vectoring the jet pair using an imposed phase difference of 150° between the jet pair

---

[1] B. L. Smith and A. Glezer, "The formation and evolution of synthetic jets," *Phys. Fluids*, **10**, 1998, pp. 2281-2297.

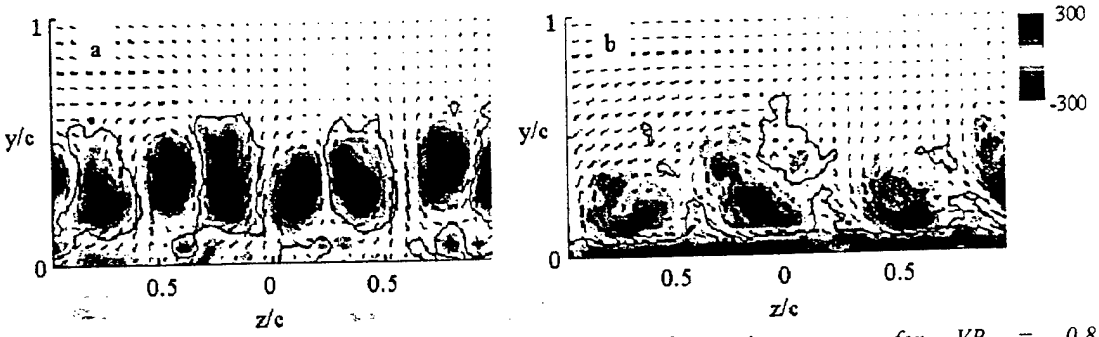

Figure 6. Cross stream vorticity contour maps of a jet array for VR = 0.8, x/c = 3 (a) Φ = 0° (b) Φ = 150° (vorticity concentrations as in Figure 5).

(Figure 6b), leads to the formation of an array of strong single-sign CCW vortices. This pattern persists in the streamwise direction and the formation of the opposite sense secondary vortices near the wall is apparently suppressed while the (primary) vortex cores remain at nearly the same elevation (although the cores are stretched).

Conclusions

We reported an initial fabrication procedure of an array of pressure sensors and microjet modulators, co-fabricated on the same substrate. The array is based on robust stainless steel shim stock, lamination processing, and stainless steel diaphragms for the pressure sensor, and stainless steel actuator discs for the microjet modulators. The sensors were successfully characterized. A study of various device geometries for the microjet modulators shows that actuation voltages can be reduced below 200 V, but with the expense of reduced jet center velocities achievable. To achieve higher actuation forces we are currently fabricating a thermally actuated bimorph structure. To achieve higher resolution and interfacing to multiple sensors an ASIC read-out circuit has been successfully designed and tested and will be co-integrated with the pressure sensor array. Arrays of streamwise vortex generators are developed using lithographic techniques. Single-sign streamwise vortices are formed by spanwise vectoring of a pair of rectangular synthetic jets issuing into a cross-flow thus providing on-demand vortex generation without alteration of surface geometry.

Acknowledgement/Disclaimer

This work was sponsored in part by the Air Force Office of Scientific Research, USAF, and by the Defense Advanced Research Projects Agency (DARPA), under grant/contract number F49620-97-1-0519. The views and conclusions contained herein are those of the authors and should not be interpreted as necessarily representing the official policies or endorsements, either expressed or implied, of the Air Force Office of Scientific Research or the U.S. Government.

Personnel

The work discussed in this report has been performed by Sung Pil Chang, Brian English, and Dr. Martin von Arx of the School of Electrical and Computer Engineering, and Chris Rinehart of the School of Mechanical Engineering, in addition to the authors.